

Chapter 1

Semianalytic Methods for Studying Localized Modes Within Two-Dimensional Photonic Crystals

The design of photonic crystal (PC) based optical elements has often relied on numerical simulations using methods such as finite-difference time-domain (FDTD) [6, 7]. While FDTD provides a wealth of detailed information about the system under consideration, it has the drawback of being rather computationally intensive and time consuming. In this chapter, I detail two approximate analytic methods that are of great use in studying planar PC cavities (fig. 1.1). The first is a group-theory-based analysis [24] that provides information about the symmetries and dominant Fourier components of defect modes within hexagonal and square lattice PC cavities. The second method [25] is a Wannier-like equation analysis that describes how the photonic lattice provides localization for the cavity modes. Taken together, these two techniques can provide approximate modal field patterns that reproduce many of the detailed features of the cavity modes generated by FDTD simulations. They thus serve as a starting point from which a more detailed analysis or optimization of the cavity design can proceed.

1.1 Symmetry-based analysis

1.1.1 Introduction

The work described in this section is largely based on ref. [24], and is presented here in a slightly different form, where I have omitted some results that are not utilized in the rest of this thesis in favor of more detailed derivations of some basic results. The principal thrust of the analysis is contained in sections 1.1.2 and 1.1.3, which outline the application of group theory in producing

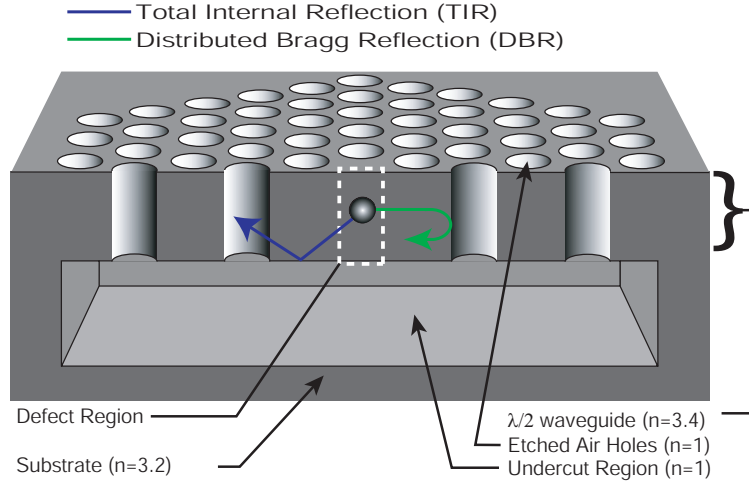


Figure 1.1: Illustration of a two-dimensional photonic crystal cavity in a slab waveguide structure.

an approximate description of the resonant modes of the defect cavities in hexagonal and square host photonic lattices. Section 1.1.4 then presents the results of FDTD simulations, confirming the results of the approximate group theory analysis while providing detailed properties of the defect mode resonances beyond the scope of the simple symmetry analysis.

The spatial symmetries within Maxwell's equations are determined by the translation and rotary-reflection symmetries of the dielectric function, $\epsilon(\mathbf{r})$ [90]. The theory of space groups [91] can then be used to predict and categorize the resonant modes of defects within PC structures. A two-step process is implemented here. First, modes of the unperturbed slab waveguide are used as a symmetry basis to generate approximate field patterns for the PC modes at the high symmetry points of the first Brillouin zone (IBZ) boundary. The curvature of the photonic bands at these points are such that peaks and valleys are created in the energy-momentum dispersion surface. It is these peaks and valleys that are the seeds from which localized states are formed. The second step in our approach then utilizes the PC band-edge states created from the unperturbed slab waveguide mode symmetry basis to generate approximate forms for the localized defect modes lying within the bandgap.

The host PC structures that we consider consist of a symmetric planar geometry with a two-dimensionally patterned core layer surrounded by spatially uniform cladding layers. A structure which has been the basis of many previously fabricated devices is depicted in cross section in fig. 1.1. The semiconductor core dielectric material has an approximate refractive index of 3.4, and the cladding in these membrane-type structures is air with a refractive index of 1. For the structures

studied in this and following sections, the ratio of the core thickness, d , to lattice constant, a , is chosen so as to maintain the single-mode nature of the vertical waveguide for wavelengths within the first-order guided-mode bandgap of the PC lattice. The modes of a symmetric slab waveguide, patterned or unpatterned, separate into modes of even or odd parity with respect to a mirror plane in the middle of the dielectric slab. Of interest here are the *fundamental* guided modes. Limiting our analysis to the fundamental guided modes of the PC slab effectively reduces the spatial dimension of the problem from three to two.

Within the mirror plane of the waveguide in these symmetric quasi-2D systems, the fundamental even and odd modes can be represented by scalar fields H_z and E_z , respectively. As has been described elsewhere [4], for connected 2D lattices such as those investigated here, the extent of the photonic bandgap for modes with electric field polarization in the plane of the 2D patterning (TE) is larger than for modes with normal electric field polarization (TM). For this reason, we will focus our attention on the fundamental even modes of the 2D PC waveguides which are TE-like (although the fundamental even and odd modes of the patterned slab are not purely TE or TM, they are significantly TE-like or TM-like in nature). An extension to TM-like modes has been presented in ref. [37], as it finds specific application in the study of quantum cascade photonic crystal lasers, due to the TM polarization of the intersubband transitions within quantum cascade heterostructures. In the analysis below, we consider two of the most common 2D geometries for the host PC lattice, the square lattice and the hexagonal or trigonal lattice. We begin with an analysis of the hexagonal lattice.

1.1.2 Hexagonal lattice photonic crystals

The point group symmetry of a 2D hexagonal PC is D_{6h} , with a single horizontal mirror plane (σ_h) lying in the waveguide center. Narrowing our scope to TE-like modes of a symmetric slab, the point group symmetry of the hexagonal PC system can be effectively reduced to $C_{6v}=D_{6h}/\sigma_h$. A plot of the approximate in-plane bandstructure for the fundamental TE-like guided modes of a half-wavelength thick hexagonally patterned slab waveguide is given in fig. 1.2(a).¹ This bandstructure was calculated through the plane wave expansion technique, as reviewed in ref. [5].

Within the mirror plane of the slab, the magnetic field pattern for the (fundamental) TE-like eigenmodes of the unpatterned slab waveguide can be written as $\mathbf{H}_{\mathbf{k}_\perp}(\mathbf{r}_\perp) = \hat{z}e^{-i(\mathbf{k}_\perp \cdot \mathbf{r}_\perp)}$, where \mathbf{k}_\perp

¹In this calculation a 2D hexagonal PC with host dielectric constant given by the effective index of the fundamental TE mode of the half-wavelength thick slab is analyzed [7].

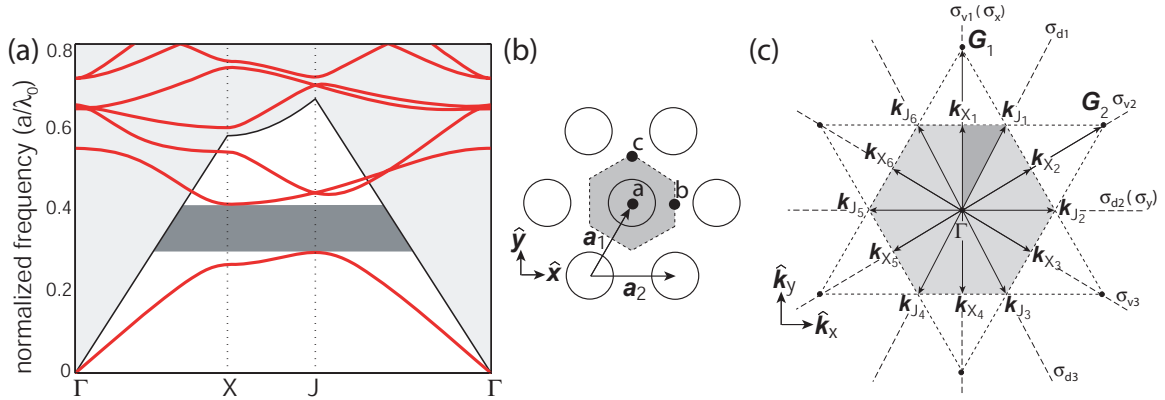


Figure 1.2: (a) Fundamental TE-like guided mode bandstructure ($r/a = 0.36$, $n_{\text{slab}} = n_{\text{eff}} = 2.65$). The bandgap extends over a normalized frequency of 0.29-0.41. The air (cladding) light line is shown as a solid black line. (b)-(c) Illustration of the real and reciprocal spaces of the two-dimensional hexagonal PC. The high-symmetry points of the hexagonal lattice, referenced to the center of an air hole, are $\mathbf{a} = (0, 0)$, $\mathbf{b} = (a/2, 0)$, and $\mathbf{c} = (0, a/\sqrt{3})$. (b) Real space. $|\mathbf{a}_1| = |\mathbf{a}_2| = a$. (c) Reciprocal space. $|\mathbf{G}_1| = |\mathbf{G}_2| = 4\pi/\sqrt{3}a$, $|\mathbf{k}_X| = 2\pi/\sqrt{3}a$, $|\mathbf{k}_J| = 4\pi/3a$.

and \mathbf{r}_\perp are in-plane wavenumber and spatial coordinates, respectively (in order to simplify notation we drop the \perp label in the equations that follow). Upon patterning the slab waveguide, coupling occurs between waveguide modes with similar unperturbed frequencies and identical propagation constants modulo a reciprocal lattice vector \mathbf{G} . This follows from the approximate conservation of frequency and the exact conservation of crystal momentum. Of particular interest for the resonant cavity designs and devices described below are those modes which comprise the frequency bands defining the first order bandgap. The Bloch modes at the band-edges defining the first order bandgap are predominantly formed from modes of the unpatterned waveguide with in-plane wavevector lying at the boundary of the IBZ; other unpatterned waveguide modes with additional in-plane momentum equal to some integer multiple of a reciprocal lattice vector contribute much less, owing to their large (unperturbed) frequency difference. For the symmetry analysis described here we will be satisfied with considering the contribution from only the degenerate lowest frequency unperturbed waveguide modes at the first zone boundary.

The high symmetry points within and on the boundary of the IBZ of the hexagonal lattice are (see fig. 1.2(c)): the six X points ($\{\pm(0, 1)k_X, \pm(\sqrt{3}/2, 1/2)k_X, \pm(\sqrt{3}/2, -1/2)k_X\}$), the six J points ($\{\pm(1/2, \sqrt{3}/2)k_J, \pm(1/2, -\sqrt{3}/2)k_J, \pm(1, 0)k_J\}$), and the Γ point $= (0, 0)$. The first-order bandgap of the hexagonal lattice (see fig. 1.2(a)) is defined from above by the X point and below by the J point. In analogy to the electronic bands in semiconductor crystals, the high frequency

Table 1.1: Point group character tables for the hexagonal lattice.

C_{6v}	E	C_2	$2C_3$	$2C_6$	$3\sigma_d$	$3\sigma_v$
A_1''	1	1	1	1	1	1
A_2''	1	1	1	1	-1	-1
B_1''	1	-1	1	-1	1	-1
B_2''	1	-1	1	-1	-1	1
E_1	2	-2	-1	1	0	0
E_2	2	2	-1	-1	0	0
$S^{a,d1}$	3	-3	0	0	1	-1
$S^{a,a1}$	2	0	2	0	-2	0
$S^{a,a2}$	3	3	0	0	-1	-1

C_{2v}	E	C_2	$\sigma_x(\sigma_{v1})$	$\sigma_y(\sigma_{d2})$
A_1	1	1	1	1
A_2	1	1	-1	-1
B_1	1	-1	-1	1
B_2	1	-1	1	-1
$S^{a,d1}$	3	-3	-1	1
$S^{b,d1}$	3	1	-1	1
$S^{a,a1}$	2	0	0	-2
$S^{a,a2}$	3	3	-1	-1
$S^{b,a1}$	3	3	-1	-1

C_{3v,σ_d}	E	$2C_3$	$3\sigma_d$	C_{3v,σ_v}	E	$2C_3$	$3\sigma_v$
A_1'	1	1	1	A_1'''	1	1	1
A_2'	1	1	-1	A_2'''	1	1	-1
E	2	-1	0	E	2	-1	0
				$S^{c,d1}$	3	0	-1
				$S^{c,a1}$	2	-1	0

band defining the first-order bandgap is called the conduction band, and the low frequency band is the valence band [4]. In the approximate analysis of the defect states to follow we will need to include all the degenerate satellite peaks (conduction band) and valleys (valence band). The group of the wavevector, which defines the point group symmetry of a plane wave modulo \mathbf{G} within the dielectric lattice, is C_{2v} , C_{3v} , and C_{6v} , for the X , J , and Γ points of the hexagonal lattice, respectively. Character tables [92] for these groups are given in table 1.1.

1.1.2.1 X-point

For the frequency bands defining the first-order bandgap, the unpatterned waveguide modes which are most strongly coupled together to form the Bloch modes at the X -point are given by $\mathbf{H} = \hat{z}e^{-i\mathbf{k}_X \cdot \mathbf{r}}$, where $i = 1, 2, \dots, 6$. The unperturbed frequencies of these modes are degenerate and can be written as $\omega_o^X \approx c|\mathbf{k}_X|/n_{\text{eff}}$, where n_{eff} is an effective index taking into account the vertical waveguiding perpendicular to the slab.

The star of \mathbf{k} ($\star\mathbf{k}$) at the X -point, formed from the independent satellite X -points within the IBZ, consists of wavevectors $\{\mathbf{k}_{X_1}, \mathbf{k}_{X_2}, \mathbf{k}_{X_3}\}$, with all other X -points being equivalent to one of these vectors modulo a reciprocal lattice vector. A symmetry basis for the modes of the patterned slab waveguide at the X_1 -satellite point can be found by applying the symmetry operations of the group of the wave vector ($G_{o\mathbf{k}_X} = C_{2v}$) to the seed vector $\mathbf{H}_{\mathbf{k}_{X_1}}$. In this case, the basis is simply $(\mathbf{H}_{\mathbf{k}_{X_1}}, \mathbf{H}_{-\mathbf{k}_{X_1}})$.

Using these basis vectors, we calculate the 2×2 matrices that represent the different point group operations of C_{2v} , noting that the magnetic field transforms like a pseudovector [93] (unlike the electric field). This yields the following:

$$S_E^X = \begin{pmatrix} 1 & 0 \\ 0 & 1 \end{pmatrix} \quad S_{C_2}^X = \begin{pmatrix} 0 & 1 \\ 1 & 0 \end{pmatrix} \quad S_{\sigma_x}^X = \begin{pmatrix} -1 & 0 \\ 0 & -1 \end{pmatrix} \quad S_{\sigma_y}^X = \begin{pmatrix} 0 & -1 \\ -1 & 0 \end{pmatrix}. \quad (1.1)$$

The character values for these operations are $\chi_E=2$, $\chi_{C_2}=0$, $\chi_{\sigma_x}=-2$, and $\chi_{\sigma_y}=0$. These character values are consistent with a reducible representation that decomposes as $A_2 \oplus B_1$. The projection operators [92] onto these IRREP spaces are calculated as:

$$P_{A_2} = \frac{1}{4} \left\{ 1 \begin{pmatrix} 1 & 0 \\ 0 & 1 \end{pmatrix} + 1 \begin{pmatrix} 0 & 1 \\ 1 & 0 \end{pmatrix} + (-1) \begin{pmatrix} -1 & 0 \\ 0 & -1 \end{pmatrix} + (-1) \begin{pmatrix} 0 & -1 \\ -1 & 0 \end{pmatrix} \right\} = \frac{1}{2} \begin{pmatrix} 1 & 1 \\ 1 & 1 \end{pmatrix} \quad (1.2)$$

$$P_{B_1} = \frac{1}{4} \left\{ 1 \begin{pmatrix} 1 & 0 \\ 0 & 1 \end{pmatrix} + (-1) \begin{pmatrix} 0 & 1 \\ 1 & 0 \end{pmatrix} + (-1) \begin{pmatrix} -1 & 0 \\ 0 & -1 \end{pmatrix} + (1) \begin{pmatrix} 0 & -1 \\ -1 & 0 \end{pmatrix} \right\} = \frac{1}{2} \begin{pmatrix} 1 & -1 \\ -1 & 1 \end{pmatrix} \quad (1.3)$$

Applying these projection operators to the seed vector $\mathbf{H}_{\mathbf{k}_{X_1}}$ yields:

$$\begin{aligned} \mathbf{H}_{A_2}^{X_1} &= \hat{z} \cos(\mathbf{k}_{X_1} \cdot \mathbf{r}^a), \\ \mathbf{H}_{B_1}^{X_1} &= \hat{z} \sin(\mathbf{k}_{X_1} \cdot \mathbf{r}^a), \end{aligned} \quad (1.4)$$

where A_2 and B_1 label the IRREP spaces of C_{2v} (see table 1.1), and the index a is used to denote the location of the origin within the hexagonal lattice (marked in fig. 1.2(b)). As the magnetic field of $\mathbf{H}_{A_2}^{X_1}$ overlaps strongly with the air holes of the hexagonal PC (its electric field lying largely in the dielectric) it represents the lower frequency ‘‘valence’’ band mode, while $\mathbf{H}_{B_1}^{X_1}$ represents the ‘‘conduction’’ band mode. This is a result of the tendency for modes with electric field concentrated within regions of high dielectric constant to be lower frequency than those with electric field concentrated in low dielectric regions [4].

In order to fully define the modes at the X -point all modes of the $\star\mathbf{k}$ must be included. In the case of the X -point this corresponds to successive rotations by $\pi/6$ (C_6 rotation). The result is the following set of degenerate valence band modes,

$$VB_a^X = \begin{pmatrix} v_{X_1} \\ v_{X_2} \\ v_{X_3} \end{pmatrix} = \hat{z} \begin{pmatrix} \cos(\mathbf{k}_{X_1} \cdot \mathbf{r}^a) \\ \cos(\mathbf{k}_{X_2} \cdot \mathbf{r}^a) \\ \cos(\mathbf{k}_{X_3} \cdot \mathbf{r}^a) \end{pmatrix}, \quad (1.5)$$

and degenerate conduction band modes,

$$CB_a^X = \begin{pmatrix} c_{X_1} \\ c_{X_2} \\ c_{X_3} \end{pmatrix} = \hat{z} \begin{pmatrix} \sin(\mathbf{k}_{X_1} \cdot \mathbf{r}^a) \\ \sin(\mathbf{k}_{X_2} \cdot \mathbf{r}^a) \\ \sin(\mathbf{k}_{X_3} \cdot \mathbf{r}^a) \end{pmatrix}. \quad (1.6)$$

fig. 1.3 shows the magnetic field amplitude for each of the valence and conduction band modes at all the satellite X -points of the hexagonal lattice.

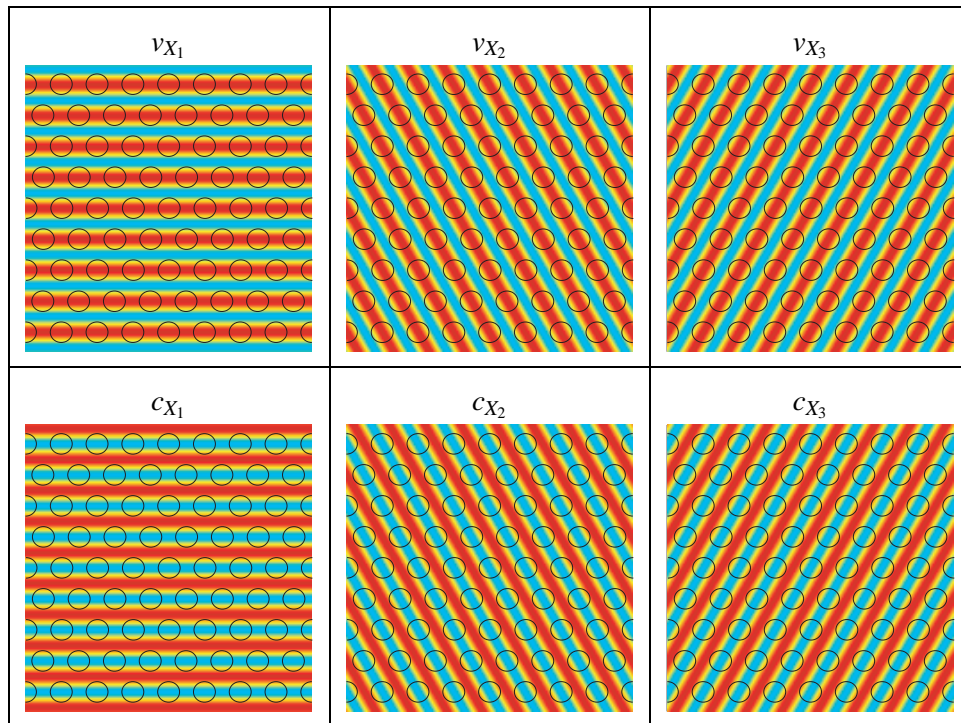


Figure 1.3: Magnetic field (amplitude) patterns of the valence band modes (top) and conduction band modes (bottom) of the hexagonal lattice at the three different X -points generated by the symmetry bases VB_a^X and CB_a^X .

1.1.2.2 J-point

A similar procedure may be performed in order to determine approximate forms for the TE-like valence and conduction band modes of the hexagonal lattice at the J -point of the IBZ. Approximate forms for the valence band edge and conduction band edge modes at the J -point are (with point a taken as the origin):

$$VB_a^J = \begin{pmatrix} v_{J_1} \\ v_{J_2} \end{pmatrix} = \hat{z} \begin{pmatrix} e^{-ik_{J_1} \cdot \mathbf{r}^a} + e^{-ik_{J_3} \cdot \mathbf{r}^a} + e^{-ik_{J_5} \cdot \mathbf{r}^a} \\ e^{-ik_{J_2} \cdot \mathbf{r}^a} + e^{-ik_{J_4} \cdot \mathbf{r}^a} + e^{-ik_{J_6} \cdot \mathbf{r}^a} \end{pmatrix}, \quad (1.7)$$

$$CB_a^J = \begin{pmatrix} c1_{J_1} \\ c2_{J_1} \\ c1_{J_2} \\ c2_{J_2} \end{pmatrix} = \hat{z} \begin{pmatrix} e^{-ik_{J_1} \cdot \mathbf{r}^a} + e^{-ik_{J_3} \cdot \mathbf{r}^a} - 2e^{-ik_{J_5} \cdot \mathbf{r}^a} \\ e^{-ik_{J_1} \cdot \mathbf{r}^a} - e^{-ik_{J_3} \cdot \mathbf{r}^a} \\ e^{-ik_{J_2} \cdot \mathbf{r}^a} + e^{-ik_{J_4} \cdot \mathbf{r}^a} - 2e^{-ik_{J_6} \cdot \mathbf{r}^a} \\ e^{-ik_{J_2} \cdot \mathbf{r}^a} - e^{-ik_{J_4} \cdot \mathbf{r}^a} \end{pmatrix}. \quad (1.8)$$

Figure 1.4 shows the magnetic field amplitude for each of the valence and conduction band modes at the J -point of the hexagonal lattice. Although not obvious from first inspection of equations (1.7) and (1.8), the plots in these two tables show that the modes of the symmetry basis VB_a^J have a magnetic field amplitude predominantly overlapping the air holes while the magnetic field amplitude of the modes of CB_a^J overlap the dielectric regions, a property that allows us to classify the modes as valence and conduction band, respectively. This result is also quite encouraging, given the fact that our symmetry basis is quite primitive and yet can reproduce this property of the valence and conduction band modes so critical to the formation of a frequency bandgap.

The approximate valence and conduction band edge modes derived above all have their origin at the center of an air hole of the lattice. The hexagonal lattice has two other high-symmetry points around which one may center a defect, points b and c shown in fig. 1.2(b). Unlike point a , points b and c are of lower symmetry than the point group of the hexagonal lattice. A defect centered about point b will be limited to a point group of symmetry C_{2v} , and those about point c to point group C_{3v, σ_v} . The point group symmetry operations for each of these types of defects are centered about different points within the lattice. So as to be clear about the position of the origin to be used for point symmetry operations, we label the Bloch mode symmetry bases with an index corresponding to the location of the origin around which it is expanded. For example, VB_b^X is the X -point valence band basis of equation (1.5) written in a shifted coordinate system with point b at the origin. In the equations to follow, \mathbf{r}^a , \mathbf{r}^b , and \mathbf{r}^c are coordinate systems with origin located at point a , b , and c of the hexagonal lattice, respectively.

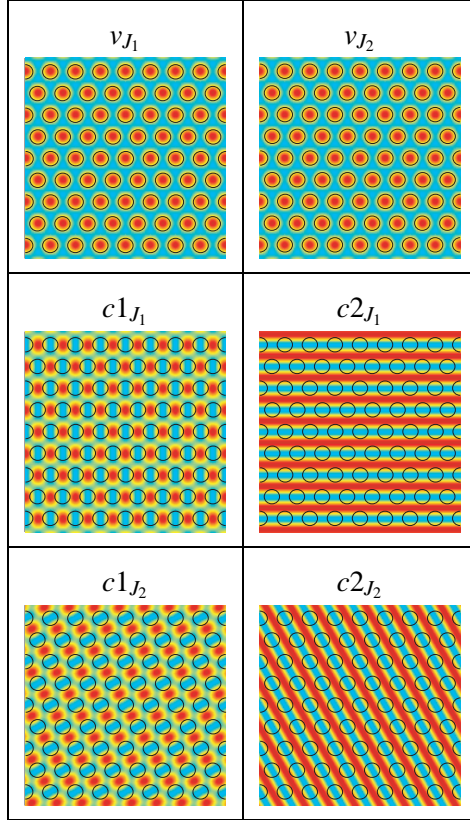


Figure 1.4: Magnetic field (amplitude) patterns of the valence band (top) and conduction band (middle and bottom) modes of the hexagonal lattice at the J -point, generated by the symmetry bases VB_a^J and CB_a^J .

1.1.2.3 Conduction band donor modes

In an attempt to form localized resonances, the dielectric constant in a small region of a periodic photonic crystal lattice may be altered from its unperturbed value, breaking the regular periodicity of the lattice and mixing the Bloch modes. If the perturbation corresponds to a local increase in the dielectric constant (fig. 1.5(a)), the localized modes are formed predominantly from the conduction band, specifically the modes at the band edge. This is a result of the tendency for mode frequencies to decrease with increasing dielectric constant [4], pulling the conduction band edge modes into the bandgap of the photonic crystal near the defect. This type of localized mode is termed a donor mode in analogy to the electronic defect states in crystalline materials [94].

For the hexagonal PC lattice the minimum in the conduction band occurs at the X -point (see fig. 1.2(a)). Therefore, the appropriate symmetry basis to use for describing localized donor modes are the degenerate conduction band edge modes of CB_a^X , CB_b^X , and CB_c^X for defect regions centered around points a , b , and c .

Let us consider the formation of conduction band donor modes within defects that maintain the full C_{6v} symmetry of the lattice. Using the symmetry basis CB_a^X , we calculate the matrix represen-

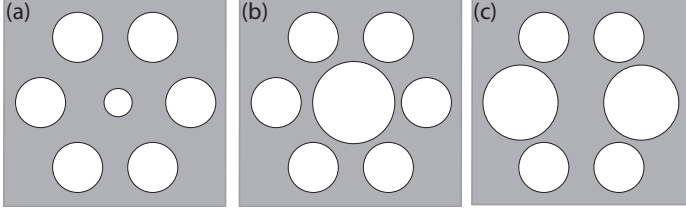


Figure 1.5: Example defect cavity geometries in the hexagonal lattice. (a) Donor-type cavity, (b) Acceptor-type cavity, (c) Y-split acceptor-type cavity.

tation of the point group operators:

$$E_{CB^x} = \begin{pmatrix} 1 & 0 & 0 \\ 0 & 1 & 0 \\ 0 & 0 & 1 \end{pmatrix} C_{2,CB^x} = \begin{pmatrix} -1 & 0 & 0 \\ 0 & -1 & 0 \\ 0 & 0 & -1 \end{pmatrix} C_{3,CB^x} = \begin{pmatrix} 0 & -1 & 0 \\ 0 & 0 & -1 \\ 1 & 0 & 0 \end{pmatrix} C_{3,CB^x}^{-1} = \begin{pmatrix} 0 & 0 & 1 \\ -1 & 0 & 0 \\ 0 & -1 & 0 \end{pmatrix} \quad (1.9)$$

$$C_{6,CB^x} = \begin{pmatrix} 0 & 0 & -1 \\ 1 & 0 & 0 \\ 0 & 1 & 0 \end{pmatrix} C_{6,CB^x}^{-1} = \begin{pmatrix} 0 & 1 & 0 \\ 0 & 0 & 1 \\ -1 & 0 & 0 \end{pmatrix} \sigma_{d_1,CB^x} = \begin{pmatrix} 0 & -1 & 0 \\ -1 & 0 & 0 \\ 0 & 0 & 1 \end{pmatrix} \sigma_{d_2,CB^x} = \begin{pmatrix} 1 & 0 & 0 \\ 0 & 0 & -1 \\ 0 & -1 & 0 \end{pmatrix} \quad (1.10)$$

$$\sigma_{d_3,CB^x} = \begin{pmatrix} 0 & 0 & 1 \\ 0 & 1 & 0 \\ 1 & 0 & 0 \end{pmatrix} \sigma_{v_1,CB^x} = \begin{pmatrix} -1 & 0 & 0 \\ 0 & 0 & 1 \\ 0 & 1 & 0 \end{pmatrix} \sigma_{v_2,CB^x} = \begin{pmatrix} 0 & 0 & -1 \\ 0 & -1 & 0 \\ -1 & 0 & 0 \end{pmatrix} \sigma_{v_3,CB^x} = \begin{pmatrix} 0 & 1 & 0 \\ 1 & 0 & 0 \\ 0 & 0 & -1 \end{pmatrix} \quad (1.11)$$

The character values for these operations are $\chi_E=3$, $\chi_{C_2}=-3$, $\chi_{C_3}=0$, $\chi_{C_6}=0$, $\chi_{\sigma_d}=1$, and $\chi_{\sigma_v}=-1$. These character values are consistent with a reducible representation that decomposes as $S^{a,d1} = E_1 \oplus B_1''$, as listed in table 1.1. For the B_1'' representation, the calculation of the projection operator is done using the same method as was used to calculate the projectors for the conduction band modes at the X-point. For the E_1 representation, there is an additional step because it is a two-dimensional representation. Recalling that E_1 can be spanned by the coordinate pair (x,y) , we write out two-

dimensional matrices for E_1 :

$$E_E = \begin{pmatrix} 1 & 0 \\ 0 & 1 \end{pmatrix} \quad E_{C_2} = \begin{pmatrix} -1 & 0 \\ 0 & -1 \end{pmatrix} \quad E_{C_3} = \begin{pmatrix} \frac{-1}{2} & \frac{\sqrt{3}}{2} \\ \frac{-\sqrt{3}}{2} & \frac{1}{2} \end{pmatrix} \quad E_{C_3^{-1}} = \begin{pmatrix} \frac{-1}{2} & \frac{-\sqrt{3}}{2} \\ \frac{\sqrt{3}}{2} & \frac{-1}{2} \end{pmatrix} \quad (1.12)$$

$$E_{C_6} = \begin{pmatrix} \frac{1}{2} & \frac{\sqrt{3}}{2} \\ \frac{-\sqrt{3}}{2} & \frac{1}{2} \end{pmatrix} \quad E_{C_6^{-1}} = \begin{pmatrix} \frac{1}{2} & \frac{-\sqrt{3}}{2} \\ \frac{\sqrt{3}}{2} & \frac{1}{2} \end{pmatrix} \quad E_{\sigma_{d1}} = \begin{pmatrix} \frac{-1}{2} & \frac{\sqrt{3}}{2} \\ \frac{\sqrt{3}}{2} & \frac{1}{2} \end{pmatrix} \quad E_{\sigma_{d2}} = \begin{pmatrix} 1 & 0 \\ 0 & -1 \end{pmatrix} \quad (1.13)$$

$$E_{\sigma_{d3}} = \begin{pmatrix} \frac{-1}{2} & \frac{-\sqrt{3}}{2} \\ \frac{-\sqrt{3}}{2} & \frac{1}{2} \end{pmatrix} \quad E_{\sigma_{v1}} = \begin{pmatrix} -1 & 0 \\ 0 & 1 \end{pmatrix} \quad E_{\sigma_{v2}} = \begin{pmatrix} \frac{1}{2} & \frac{\sqrt{3}}{2} \\ \frac{\sqrt{3}}{2} & \frac{-1}{2} \end{pmatrix} \quad E_{\sigma_{v3}} = \begin{pmatrix} \frac{1}{2} & \frac{-\sqrt{3}}{2} \\ \frac{-\sqrt{3}}{2} & \frac{1}{2} \end{pmatrix} \quad (1.14)$$

The diagonal elements of these matrices are then used in the calculation of the two projectors within this subspace. Overall, we arrive at the following projection operators for the conduction band donor modes:

$$P_{B'_1}^{CB^X} = \frac{1}{3} \begin{pmatrix} 1 & -1 & 1 \\ -1 & 1 & -1 \\ 1 & -1 & 1 \end{pmatrix} \quad P_{E_{1,1}}^{CB^X} = \frac{1}{6} \begin{pmatrix} 4 & 2 & -2 \\ 2 & 1 & -1 \\ -2 & -1 & 1 \end{pmatrix} \quad P_{E_{1,2}}^{CB^X} = \frac{1}{2} \begin{pmatrix} 0 & 0 & 0 \\ 0 & 1 & 1 \\ 0 & 1 & 1 \end{pmatrix} \quad (1.15)$$

Note that the coefficients in front of these projection matrices are eventually dropped as the approximate solutions that we give are not absolutely normalized, although the relative amplitudes of the different Fourier components are certainly kept (and are captured by the projection matrices themselves, without the prefactors). Using these projection operators on CB_a^X , a set of basis functions for the localized conduction band donor modes centered about point a of the hexagonal lattice is found:

$$\begin{aligned}
\mathbf{H}_{B_1''}^{a,d1} &= \hat{z} \left(\sin(\mathbf{k}_{X_1} \cdot \mathbf{r}^a) - \sin(\mathbf{k}_{X_2} \cdot \mathbf{r}^a) + \sin(\mathbf{k}_{X_3} \cdot \mathbf{r}^a) \right) \\
\mathbf{H}_{E_{1,1}}^{a,d1} &= \hat{z} \left(2 \sin(\mathbf{k}_{X_1} \cdot \mathbf{r}^a) + \sin(\mathbf{k}_{X_2} \cdot \mathbf{r}^a) - \sin(\mathbf{k}_{X_3} \cdot \mathbf{r}^a) \right) \\
\mathbf{H}_{E_{1,2}}^{a,d1} &= \hat{z} \left(\sin(\mathbf{k}_{X_2} \cdot \mathbf{r}^a) + \sin(\mathbf{k}_{X_3} \cdot \mathbf{r}^a) \right),
\end{aligned} \tag{1.16}$$

Similar techniques are used to find the character values of representation $S^{b,d1}$ of the CB_b^X basis under C_{2v} and representation $S^{c,d1}$ of the CB_c^X basis under $C_{3v,\sigma}$, and they are given in table 1.1. From the character tables we find that these representations decompose as $S^{b,d1} = A_1 \oplus A_2 \oplus B_1$ and $S^{c,d1} = E \oplus A_2'''$. We then use the appropriate projection operators to find basis functions for the localized conduction band donor modes centered about point b :

$$\begin{aligned}
\mathbf{H}_{A_1}^{b,d1} &= \hat{z} \left(\cos(\mathbf{k}_{X_2} \cdot \mathbf{r}^b) - \cos(\mathbf{k}_{X_3} \cdot \mathbf{r}^b) \right) \\
\mathbf{H}_{A_2}^{b,d1} &= \hat{z} \left(\cos(\mathbf{k}_{X_2} \cdot \mathbf{r}^b) + \cos(\mathbf{k}_{X_3} \cdot \mathbf{r}^b) \right) \\
\mathbf{H}_{B_1}^{b,d1} &= \hat{z} \left(\sin(\mathbf{k}_{X_1} \cdot \mathbf{r}^b) \right),
\end{aligned} \tag{1.17}$$

and point c :

$$\begin{aligned}
\mathbf{H}_{A_2'''}^{c,d1} &= \hat{z} \left(\sin\left(\mathbf{k}_{X_1} \cdot \mathbf{r}^c - \frac{\pi}{3}\right) - \sin\left(\mathbf{k}_{X_2} \cdot \mathbf{r}^c + \frac{\pi}{3}\right) \right. \\
&\quad \left. + \sin\left(\mathbf{k}_{X_3} \cdot \mathbf{r}^c - \frac{\pi}{3}\right) \right) \\
\mathbf{H}_{E_{1,1}}^{c,d1} &= \hat{z} \left(2 \sin\left(\mathbf{k}_{X_1} \cdot \mathbf{r}^c - \frac{\pi}{3}\right) + \sin\left(\mathbf{k}_{X_2} \cdot \mathbf{r}^c + \frac{\pi}{3}\right) \right. \\
&\quad \left. - \sin\left(\mathbf{k}_{X_3} \cdot \mathbf{r}^c - \frac{\pi}{3}\right) \right) \\
\mathbf{H}_{E_{1,2}}^{c,d1} &= \hat{z} \left(\sin\left(\mathbf{k}_{X_2} \cdot \mathbf{r}^c + \frac{\pi}{3}\right) + \sin\left(\mathbf{k}_{X_3} \cdot \mathbf{r}^c - \frac{\pi}{3}\right) \right),
\end{aligned} \tag{1.18}$$

Figure 1.6 shows plots of the amplitude of the \hat{z} -component of the magnetic field for each of the localized donor modes centered about point a , as generated by the symmetry analysis. In these plots (and in all plots generated from the symmetry analysis to follow), the localization of each mode has been taken into account by multiplying a two-dimensional Gaussian envelope function with each

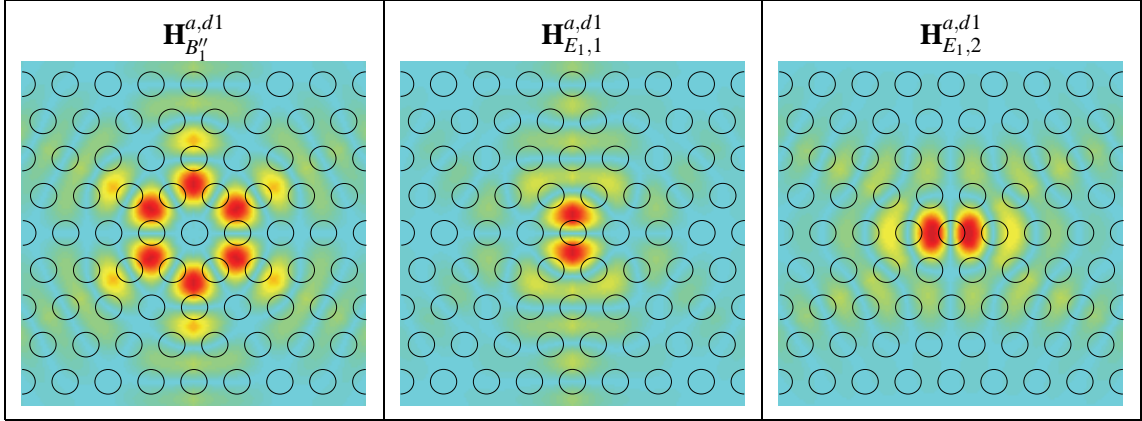


Figure 1.6: Magnetic field amplitude of the symmetry analysis conduction band donor modes centered about point a of the hexagonal lattice.

dominant Fourier component, where the two axes of the Gaussian envelope are taken as parallel and perpendicular to the direction of the Fourier component. This set of envelope function transforms as the identity under symmetry operations of the group of the wavevector, and as such does not alter the transformation properties of each \mathbf{k} component. Consequently, the IRREP classification of the defect modes given above is maintained. This particular choice of envelope function, apart from symmetry, is rather arbitrary, only chosen to capture the localized nature of the defect modes and highlight the dominant Fourier components. In section 1.2, a Wannier-like equation for the envelope of localized photon states is studied and shown to have ground state solutions invariant under those elements of the group of the wavevector that are also symmetries of the defect perturbation. The ground state envelope solutions then leave the IRREP classification of the above analysis for the defect modes unchanged.

Returning to equation (1.16) describing the localized donor modes about point a of the hexagonal lattice, we note that the $(d1, B_1'')$ donor mode transforms like a hexapole, whereas the degenerate $(d1, E_1)$ modes transform as an (x, y) -dipole pair. By introducing defect regions with lower symmetry than the host photonic lattice one is able to remove degeneracies in the localized mode spectrum. The effects of this symmetry lowering can be simply determined using group theory by virtue of the compatibility relations between the IRREPs of the full and reduced symmetry groups:

$$\begin{aligned}
C_{6v} &\rightarrow C_{2v} \\
\mathbf{H}_{B_1''}^{a,d1} &\rightarrow \mathbf{H}_{B_1}^{a,d1,1} \\
\mathbf{H}_{E_{1,1}}^{a,d1} &\rightarrow \mathbf{H}_{B_1}^{a,d1,2} \text{ (}x\text{-dipole)} \\
\mathbf{H}_{E_{1,2}}^{a,d1} &\rightarrow \mathbf{H}_{B_2}^{a,d1} \text{ (}y\text{-dipole)}.
\end{aligned} \tag{1.19}$$

In the case of cavities with C_{2v} symmetry, group theory predicts the splitting of the degenerate dipole-like modes into x and y dipole-like modes with differing frequencies. This has been studied in numerical simulations and experimental measurements of such devices [2].

1.1.2.4 Valence band acceptor modes

If the dielectric constant had been reduced in a small region within the photonic lattice, by enlarging an air hole for instance (fig. 1.5(b)), then instead of pulling the conduction band modes down into the photonic crystal bandgap the valence band modes are pushed up into the bandgap. In this case modes localized to the defect region are formed predominantly from mixtures of Bloch modes from the valence band edge. This type of defect mode is termed an acceptor mode, again in analogy to the electronic states in a crystal [94]. For the hexagonal lattice the maximum of the valence band occurs at the J -point (see fig. 1.2(a)). The obvious symmetry basis to use to describe the acceptor modes is the set of degenerate valence band modes at the J -point, VB_a^J in the case of defects centered around point a , and VB_b^J and VB_c^J for defects about points b and c , respectively.

The characters of the representation $S^{a,a1}$ of VB_a^J under the C_{6v} point symmetry group, the representation $S^{b,a1}$ of VB_b^J under C_{2v} , and the representation $S^{c,a1}$ of VB_c^J under C_{3v,σ_v} are given in table 1.1. $S^{a,a1}$ decomposes into irreducible blocks $A_2'' \oplus B_2''$, $S^{b,a1} = A_2 \oplus B_2$, and $S^{c,a1} = E$. Using the projection operators, the basis functions VB_a^J are coupled together to form the following acceptor modes about point a :

$$\begin{aligned}
\mathbf{H}_{A_2''}^{a,a1} &= \hat{z} \left(\cos(\mathbf{k}_{J_1} \cdot \mathbf{r}^a) + \cos(\mathbf{k}_{J_3} \cdot \mathbf{r}^a) + \cos(\mathbf{k}_{J_5} \cdot \mathbf{r}^a) \right) \\
\mathbf{H}_{B_2''}^{a,a1} &= \hat{z} \left(\sin(\mathbf{k}_{J_1} \cdot \mathbf{r}^a) + \sin(\mathbf{k}_{J_3} \cdot \mathbf{r}^a) + \sin(\mathbf{k}_{J_5} \cdot \mathbf{r}^a) \right).
\end{aligned} \tag{1.20}$$

Similarly, projecting the basis functions VB_b^J onto the IRREPs of C_{2v} and the basis functions VB_c^J

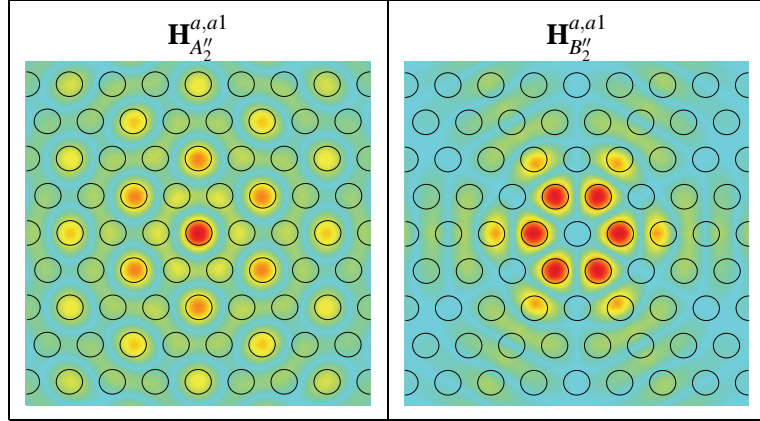


Figure 1.7: Magnetic field amplitude of the symmetry analysis valence band acceptor modes centered about point a of the hexagonal lattice.

onto the IRREPs of C_{3v,σ_v} , we get for the acceptor modes about point b :

$$\begin{aligned}\mathbf{H}_{A_2}^{b,a1} &= \hat{z} \left(\cos(\mathbf{k}_{J_1} \cdot \mathbf{r}^b) + \cos(\mathbf{k}_{J_3} \cdot \mathbf{r}^b) - \cos(\mathbf{k}_{J_5} \cdot \mathbf{r}^b) \right) \\ \mathbf{H}_{B_2}^{b,a1} &= \hat{z} \left(\sin(\mathbf{k}_{J_1} \cdot \mathbf{r}^b) + \sin(\mathbf{k}_{J_3} \cdot \mathbf{r}^b) - \sin(\mathbf{k}_{J_5} \cdot \mathbf{r}^b) \right),\end{aligned}\tag{1.21}$$

and the acceptor modes about point c :

$$\begin{aligned}\mathbf{H}_{E,1}^{c,a1} &= \hat{z} \left(\cos\left(\mathbf{k}_{J_1} \cdot \mathbf{r}^c + \frac{2\pi}{3}\right) + \cos\left(\mathbf{k}_{J_3} \cdot \mathbf{r}^c - \frac{2\pi}{3}\right) \right. \\ &\quad \left. + \cos(\mathbf{k}_{J_5} \cdot \mathbf{r}^c) \right) \\ \mathbf{H}_{E,2}^{c,a1} &= \hat{z} \left(\sin\left(\mathbf{k}_{J_1} \cdot \mathbf{r}^c + \frac{2\pi}{3}\right) + \sin\left(\mathbf{k}_{J_3} \cdot \mathbf{r}^c - \frac{2\pi}{3}\right) \right. \\ &\quad \left. + \sin(\mathbf{k}_{J_5} \cdot \mathbf{r}^c) \right).\end{aligned}\tag{1.22}$$

Figure 1.7 shows plots of the \hat{z} -component of the magnetic field for each of the localized acceptor modes centered about point a of the hexagonal lattice generated by the symmetry analysis.

In modified cavities with C_{2v} symmetry, $\mathbf{H}_{A_2''}^{a,a1}$ and $\mathbf{H}_{B_2''}^{a,a1}$ transform as A_2 and B_2 IRREPs, respectively:

$$\begin{aligned}
C_{6v} &\rightarrow C_{2v} \\
\mathbf{H}_{A_2'}^{a,a1} &\rightarrow \mathbf{H}_{A_2}^{a,a1}, \\
\mathbf{H}_{B_2'}^{a,a1} &\rightarrow \mathbf{H}_{B_2}^{a,a1}.
\end{aligned} \tag{1.23}$$

For defect regions that strongly perturb the photonic lattice it is possible that a larger number of localized defect modes will form than can be described by the limited symmetry basis used above. This is the case for the Y -split cavity described in ref. [24] and illustrated in fig. 1.5(c), where the defect region is composed of two enlarged holes and has a relatively deep potential well for acceptor modes. As a result, in the FDTD simulations of the Y -split cavity, an additional shallow acceptor type mode (Y - A_{20}), not covered by the VB_a^J symmetry basis, is present.

In order to more fully capture the possible defect modes in a deep potential well, the symmetry basis can be expanded in a number of ways [24]. The method we adopt here is based upon the observation that, for defect regions which provide a deep potential well, it is possible that defect modes will form which are composed of unperturbed photonic crystal modes located not just at the edge of the bandgap, but also at other nearby (in frequency) high-symmetry k -points within the IBZ. In order to represent these additional localized resonant modes the unperturbed photonic crystal modes at the additional high-symmetry k -points must be included in the symmetry basis. For the hexagonal lattice the valence band at the X -point is close in frequency to the bandgap edge at the J -point (see fig. 1.2(a)). The symmetry basis for the X -point valence band edge is the triply degenerate VB_a^X basis set. The representation of VB_a^X under C_{6v} , labeled $S^{a,a2}$, has the character values shown in table 1.1 and decomposes into irreducible spaces E_2 and A_2'' . The acceptor type modes formed from the X -point valence band modes in a symmetric defect cavity centered about point a in the lattice are:

$$\begin{aligned}
\mathbf{H}_{A_2''}^{a,a2} &= \hat{z} \left(\cos(\mathbf{k}_{X_1} \cdot \mathbf{r}^a) + \cos(\mathbf{k}_{X_2} \cdot \mathbf{r}^a) + \cos(\mathbf{k}_{X_3} \cdot \mathbf{r}^a) \right), \\
\mathbf{H}_{E_2,1}^{a,a2} &= \hat{z} \left(2 \cos(\mathbf{k}_{X_1} \cdot \mathbf{r}^a) - \cos(\mathbf{k}_{X_2} \cdot \mathbf{r}^a) - \cos(\mathbf{k}_{X_3} \cdot \mathbf{r}^a) \right), \\
\mathbf{H}_{E_2,2}^{a,a2} &= \hat{z} \left(\cos(\mathbf{k}_{X_2} \cdot \mathbf{r}^a) - \cos(\mathbf{k}_{X_3} \cdot \mathbf{r}^a) \right).
\end{aligned} \tag{1.24}$$

The Y -split cavity does not have C_{6v} symmetry, but rather C_{2v} symmetry. This reduction of

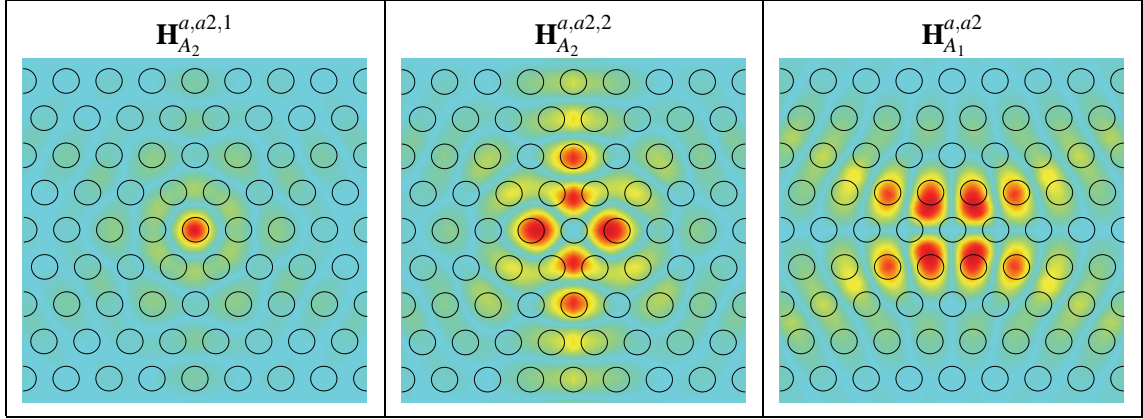


Figure 1.8: Magnetic field amplitude of the symmetry analysis acceptor modes formed from the valence band modes at the X -point of the hexagonal lattice.

symmetry causes the E_2 IRREP space to split into $A_1 \oplus A_2$, and the A_2'' space to transfer over into an A_2 IRREP space:

$$\begin{aligned}
 C_{6v} &\rightarrow C_{2v} \\
 \mathbf{H}_{A_2''}^{a,a2} &\rightarrow \mathbf{H}_{A_2}^{a,a2,1}, \\
 \mathbf{H}_{E_2,1}^{a,a2} &\rightarrow \mathbf{H}_{A_2}^{a,a2,2}, \\
 \mathbf{H}_{E_2,2}^{a,a2} &\rightarrow \mathbf{H}_{A_1}^{a,a2}.
 \end{aligned} \tag{1.25}$$

Figure 1.8 shows the magnetic field patterns of the acceptor modes predicted by the symmetry analysis to form out of the valence band at the X -point. The shallow acceptor mode ($Y-A2_0$) found in FDTD simulations of the Y -split cavity [24] transforms as the A_2 IRREP under C_{2v} symmetry operations. The dominant Fourier component within the FDTD generated field pattern of $Y-A2_0$ is \mathbf{k}_{X_1} , from which we can conclude that this mode is given by $\mathbf{H}_{A_2}^{a,a2,2}$ as opposed to $\mathbf{H}_{A_2}^{a,a2,1}$.

1.1.3 Square lattice photonic crystals

As with the hexagonal lattice we concern ourselves here with only the fundamental even modes (TE-like) of the slab waveguide. The point group symmetry of the square lattice photonic crystal can then be reduced to $C_{4v}=D_{4h}/\sigma_h$. A plot of the approximate in-plane bandstructure for the fundamental TE-like guided modes of a half-wavelength thick slab waveguide with a square array patterning of air holes is given in fig. 1.9(a).

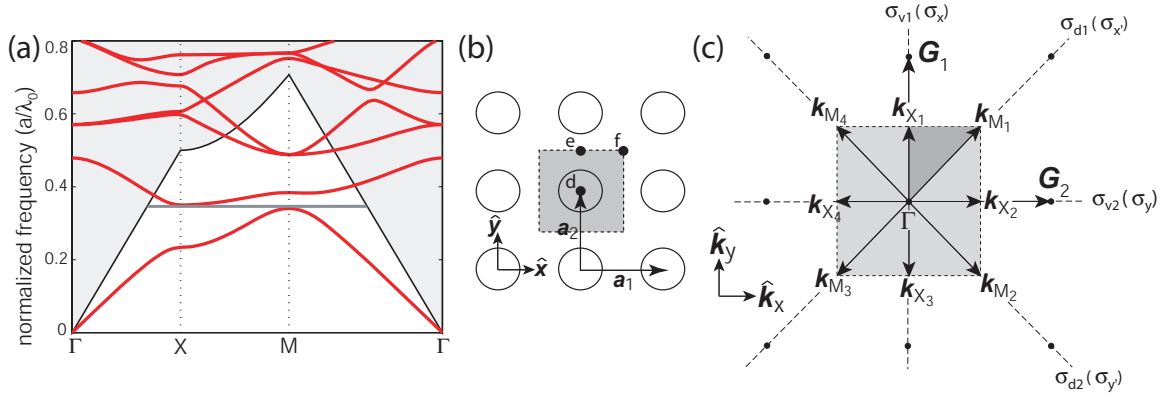


Figure 1.9: (a) Fundamental TE-like guided mode bandstructure ($r/a = 0.35$, $n_{\text{slab}} = n_{\text{eff}} = 2.65$) for a square lattice of air holes. The bandgap is seen to be much smaller for the square lattice than in the case of the hexagonal lattice. The air (cladding) light line is shown as a solid black line. (b)-(c) Illustration of the real and reciprocal spaces of the two-dimensional PC with a square array of air holes. The high-symmetry points of the square lattice, referenced to the center of an air hole, are $\mathbf{d} = (0, 0)$, $\mathbf{e} = (0, a/2)$, and $\mathbf{f} = (a/2, a/2)$. (b) Real space. $|\mathbf{a}_1| = |\mathbf{a}_2| = a$. (c) Reciprocal space. $|\mathbf{G}_1| = |\mathbf{G}_2| = 2\pi/a$, $|\mathbf{k}_X| = \pi/a$, $|\mathbf{k}_M| = \sqrt{2}\pi/a$.

The high symmetry points on the boundary or within the IBZ are (see fig. 1.9(c)): the four X points ($\{\pm(1, 0)k_X, \pm(0, 1)k_X\}$), the four M points ($(\pm\sqrt{2}/2, \pm\sqrt{2}/2)k_M$), and the Γ point $= (0, 0)$. The first-order band edges of the square lattice (see fig. 1.9(a)) are defined from above by the X point (conduction band edge) and below by the M point (valence band edge). The group of the wave vector at the X , M , and Γ points is C_{2v} , C_{4v} , and C_{4v} , respectively. Character tables [92] for the two groups are given in table 1.2.

1.1.3.1 X-point

A symmetry basis for the modes of the square lattice PC at the X -point can be found by applying the symmetry operations of the group of the wave vector ($G_{\mathbf{k}_X} = C_{2v}$) to the seed vector $\mathbf{H}_{\mathbf{k}_{X_1}}$. In this case, the basis is simply $(\mathbf{H}_{\mathbf{k}_{X_1}}, \mathbf{H}_{-\mathbf{k}_{X_1}})$. Projecting this symmetry basis onto the IRREP spaces of C_{2v} yields:

$$\begin{aligned} \mathbf{H}_{A_2}^{X_1} &= \hat{z} \cos(\mathbf{k}_{X_1} \cdot \mathbf{r}) \\ \mathbf{H}_{B_1}^{X_1} &= \hat{z} \sin(\mathbf{k}_{X_1} \cdot \mathbf{r}), \end{aligned} \quad (1.26)$$

where A_2 and B_1 label the IRREP spaces of C_{2v, σ_v} (see table 1.2). With the origin at the center of an

Table 1.2: Point group character tables for the square lattice.

C_{4v}	E	C_2	$2C_4$	$2\sigma_v$	$2\sigma_d$
A_1''	1	1	1	1	1
A_2''	1	1	1	-1	-1
B_1''	1	1	-1	1	-1
B_2''	1	1	-1	-1	1
E	2	-2	0	0	0
S^M	4	0	0	0	-2
$S^{d,d1}$	2	-2	0	0	0
$S^{f,d1}$	2	2	0	-2	0

C_{2v,σ_d}	E	C_2	$\sigma_{x'}(\sigma_{d1})$	$\sigma_{y'}(\sigma_{d2})$
A_1'	1	1	1	1
A_2'	1	1	-1	-1
B_1'	1	-1	-1	1
B_2'	1	-1	1	-1

C_{2v,σ_v}	E	C_2	$\sigma_x(\sigma_{v1})$	$\sigma_y(\sigma_{v2})$
A_1	1	1	1	1
A_2	1	1	-1	-1
B_1	1	-1	-1	1
B_2	1	-1	1	-1
S^{X1}	2	0	0	-2
$S^{e,d1}$	2	0	0	-2

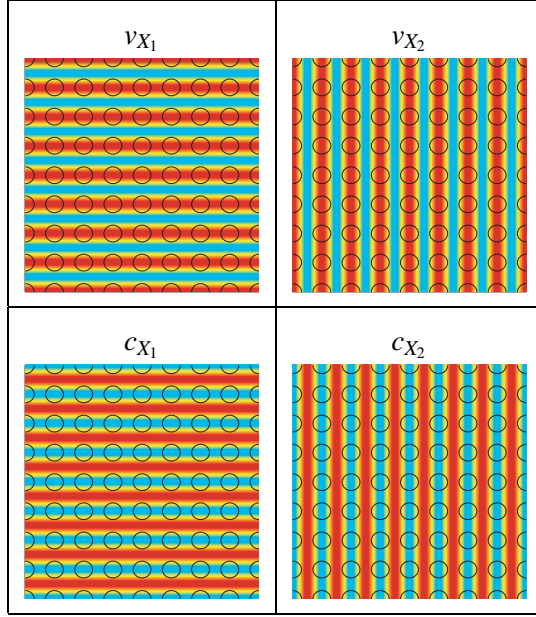


Figure 1.10: Magnetic field (amplitude) patterns of the valence band (top) and conduction band (bottom) modes of the square lattice at the X -points of the IBZ, generated by the symmetry basis VB_d^X and CB_d^X .

air hole of the lattice (point d of fig. 1.9), $\mathbf{H}_{A_2}^{X_1}$ corresponds to the “valence” band mode and $\mathbf{H}_{B_1}^{X_1}$ to the “conduction” band mode.

In order to fully define the modes at the X -point all modes of the $\star\mathbf{k}$ must be included. The result is the following set of degenerate valence band modes,

$$VB_d^X = \begin{pmatrix} v_{X_1} \\ v_{X_2} \end{pmatrix} = \hat{z} \begin{pmatrix} \cos(\mathbf{k}_{X_1} \cdot \mathbf{r}^d) \\ \cos(\mathbf{k}_{X_2} \cdot \mathbf{r}^d) \end{pmatrix}, \quad (1.27)$$

and degenerate conduction band modes,

$$CB_d^X = \begin{pmatrix} c_{X_1} \\ c_{X_2} \end{pmatrix} = \hat{z} \begin{pmatrix} \sin(\mathbf{k}_{X_1} \cdot \mathbf{r}^d) \\ \sin(\mathbf{k}_{X_2} \cdot \mathbf{r}^d) \end{pmatrix}. \quad (1.28)$$

The magnetic field amplitude patterns of the approximate valence and conduction band modes of the square lattice at the X -points of the IBZ are given in fig. 1.10.

1.1.3.2 M-point

A similar procedure may be performed in order to determine approximate forms for the TE-like valence and conduction band modes at the M -point of the IBZ. The symmetry basis, S^M , in this case includes all the M -points of the IBZ, $S^M = (\mathbf{H}_{\mathbf{k}_{M_1}}, \mathbf{H}_{\mathbf{k}_{M_2}}, \mathbf{H}_{-\mathbf{k}_{M_1}}, \mathbf{H}_{-\mathbf{k}_{M_2}})$. As determined from its character under C_{4v} (table 1.2), $S^M = E \oplus A_2'' \oplus B_1''$. The doubly degenerate IRREP E must represent a higher energy level band as the conduction and valence band edges are non-degenerate at the M -point as shown in fig. 1.9(a). Using only the A_2'' and B_1'' IRREPs, an approximate form for the valence band edge and conduction band edge modes at the M -point are calculated by projecting the symmetry basis onto these IRREP spaces. With the origin centered at point d , the valence and conduction band edge modes are:

$$VB_d^M = \begin{pmatrix} v_M \end{pmatrix} = \hat{z} \begin{pmatrix} \cos(\mathbf{k}_{M_1} \cdot \mathbf{r}^d) + \cos(\mathbf{k}_{M_2} \cdot \mathbf{r}^d) \end{pmatrix} \quad (1.29)$$

$$CB_d^M = \begin{pmatrix} c1_M \end{pmatrix} = \hat{z} \begin{pmatrix} \cos(\mathbf{k}_{M_1} \cdot \mathbf{r}^d) - \cos(\mathbf{k}_{M_2} \cdot \mathbf{r}^d) \end{pmatrix}. \quad (1.30)$$

Approximate modes for the degenerate higher frequency conduction bands represented by the IRREP E are, in one particular basis,

$$CB_d^{M,2} = \begin{pmatrix} c2_M \\ c3_M \end{pmatrix} = \hat{z} \begin{pmatrix} \sin(\mathbf{k}_{M_1} \cdot \mathbf{r}^d) - \sin(\mathbf{k}_{M_2} \cdot \mathbf{r}^d) \\ \sin(\mathbf{k}_{M_1} \cdot \mathbf{r}^d) + \sin(\mathbf{k}_{M_2} \cdot \mathbf{r}^d) \end{pmatrix}. \quad (1.31)$$

These higher frequency bands will be unimportant in our present analysis where we focus on the band edge modes defining the first order bandgap. The magnetic field amplitude patterns of the valence and conduction band modes at the M -point of the IBZ of the square lattice are given in fig. 1.11.

In the square lattice there are three different high-symmetry points around which one may center a defect. These points are labeled d , e , and f in fig. 1.9. Points d and f maintain the C_{4v} point group of the square lattice, and point e has a lowered symmetry given by the point group C_{2v,σ_v} . As was done for the hexagonal lattice, Bloch mode symmetry bases written with their origin at points d , e ,

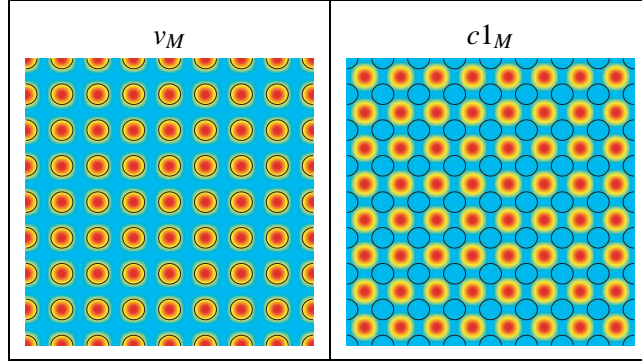


Figure 1.11: Magnetic field (amplitude) patterns of the valence and conduction band modes of the square lattice at the M -points of the IBZ generated by the symmetry analysis (VB_d^M and CB_d^M).

or f will be indexed as such. Coordinates centered about points d , e , and f of the lattice are also labeled as \mathbf{r}^d , \mathbf{r}^e , and \mathbf{r}^f , respectively.

1.1.3.3 Conduction band donor modes

For the square PC lattice the minimum in the conduction band occurs at the X -point (fig. 1.9(a)). The representations describing how the CB_d^X , CB_e^X , and CB_f^X symmetry bases transform under the appropriate point group are given by $S^{d,d1}$, $S^{e,d1}$, and $S^{f,d1}$, respectively. From their characters in table 1.2 we find that $S^{d,d1} = E$, $S^{e,d1} = A2 \oplus B2$, and $S^{f,d1} = A_2'' \oplus B_2''$. Projecting the symmetry bases onto the different IRREPs gives the following conduction band donor modes:

$$\begin{aligned} \mathbf{H}_{E,1}^{d,d1} &= \hat{z} \left(\sin(\mathbf{k}_{X_1} \cdot \mathbf{r}^d) \right) \\ \mathbf{H}_{E,2}^{d,d1} &= \hat{z} \left(\sin(\mathbf{k}_{X_2} \cdot \mathbf{r}^d) \right), \end{aligned} \quad (1.32)$$

centered about point d ,

$$\begin{aligned} \mathbf{H}_{A2}^{e,d1} &= \hat{z} \left(\cos(\mathbf{k}_{X_1} \cdot \mathbf{r}^e) \right) \\ \mathbf{H}_{B2}^{e,d1} &= \hat{z} \left(\sin(\mathbf{k}_{X_2} \cdot \mathbf{r}^e) \right), \end{aligned} \quad (1.33)$$

centered about point e , and

$$\begin{aligned}
\mathbf{H}_{A_2''}^{f,d1} &= \hat{z} \left(\cos(\mathbf{k}_{X_1} \cdot \mathbf{r}^f) + \cos(\mathbf{k}_{X_2} \cdot \mathbf{r}^f) \right) \\
\mathbf{H}_{B_2''}^{f,d1} &= \hat{z} \left(\cos(\mathbf{k}_{X_1} \cdot \mathbf{r}^f) - \cos(\mathbf{k}_{X_2} \cdot \mathbf{r}^f) \right),
\end{aligned} \tag{1.34}$$

centered about point f .

For the points d and f , defects may be formed with lower symmetry than the C_{4v} symmetry of the square lattice. We may use the compatibility relations between the IRREPs of the full and reduced symmetry groups to determine the new mode structure. For a defect of C_{2v} symmetry with mirror planes along the \hat{x} and \hat{y} directions of fig. 1.9(a) (C_{2v,σ_v}) we have the following reduction:

$$\begin{aligned}
C_{4v} &\rightarrow C_{2v,\sigma_v} \\
\mathbf{H}_{E,1}^{d,d1} &\rightarrow \mathbf{H}_{B_1}^{d,d1} \text{ (x-dipole)} \\
\mathbf{H}_{E,2}^{d,d1} &\rightarrow \mathbf{H}_{B_2}^{d,d1} \text{ (y-dipole)} \\
\mathbf{H}_{A_2''}^{f,d1} &\rightarrow \mathbf{H}_{A_2}^{f,d1,1} \\
\mathbf{H}_{B_2''}^{f,d1} &\rightarrow \mathbf{H}_{A_2}^{f,d1,2}.
\end{aligned} \tag{1.35}$$

If instead, the defect at points d and f contain the mirror planes σ_d , the symmetry is C_{2v,σ_d} and the compatibility relations give a mode decomposition:

$$\begin{aligned}
C_{4v} &\rightarrow C_{2v,\sigma_d} \\
\mathbf{H}_{E,1}^{d,d1} + \mathbf{H}_{E,2}^{d,d1} &\rightarrow \mathbf{H}_{B_1'}^{d,d1} \text{ (x'-dipole)} \\
\mathbf{H}_{E,1}^{d,d1} - \mathbf{H}_{E,2}^{d,d1} &\rightarrow \mathbf{H}_{B_2'}^{d,d1} \text{ (y'-dipole)} \\
\mathbf{H}_{A_2''}^{f,d1} &\rightarrow \mathbf{H}_{A_2'}^{f,d1} \\
\mathbf{H}_{B_2''}^{f,d1} &\rightarrow \mathbf{H}_{A_1'}^{f,d1}.
\end{aligned} \tag{1.36}$$

Magnetic field patterns of the different localized donor-type defect modes formed about point d , e , and f of the square lattice are given in fig. 1.12, where we have chosen to decompose the fields according to C_{2v,σ_v} .

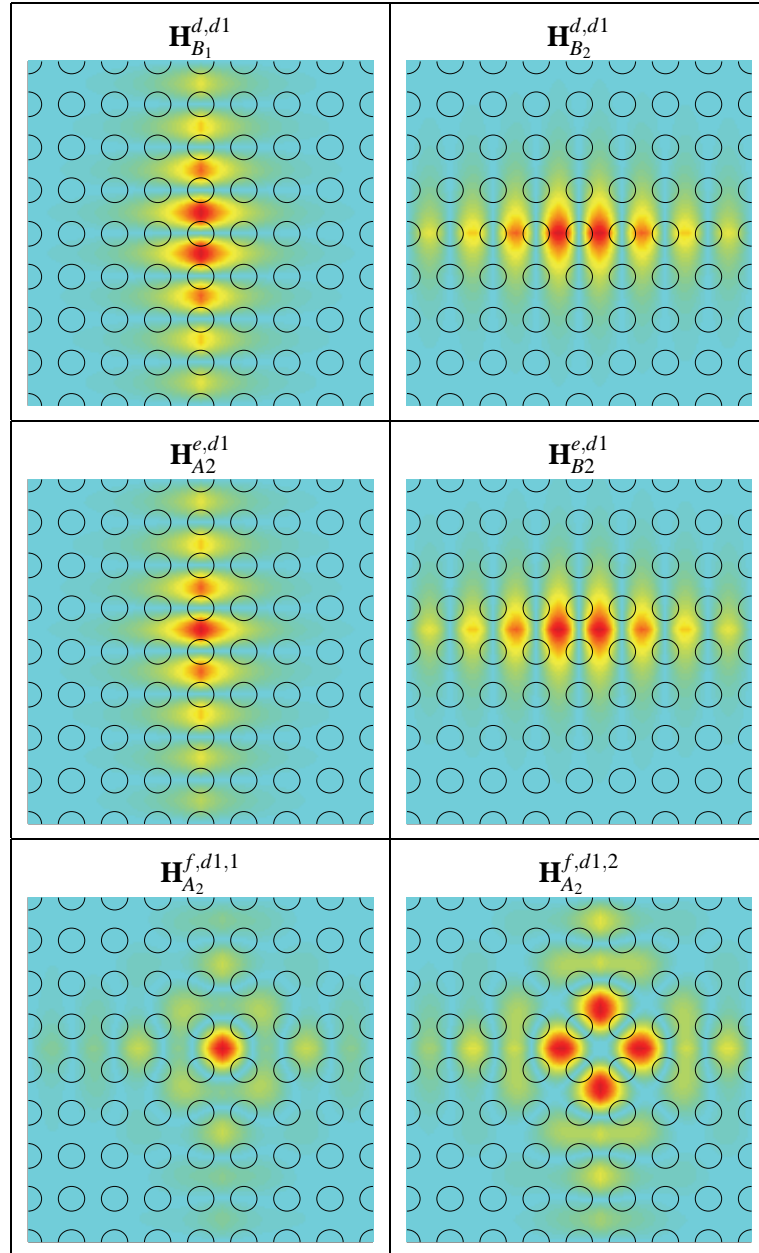


Figure 1.12: Magnetic field amplitude of the localized donor modes centered about points d , e , and f of the square lattice.

1.1.3.4 Valence band acceptor modes

For the square lattice the maximum of the valence band occurs at the M -point (fig. 1.9(a)). For the square lattice the valence band edge modes at the M -point consist of a single non-degenerate mode. This can be traced back to the fact that the M -point in the square lattice is highly symmetric, and the group of the wave vector mixes all four of the M -points on the IBZ boundary. The symmetries and fundamental momentum components of the possible acceptor modes formed from the M -point band edge modes (the approximate defect modes) are then trivially given by the single M -point valence band edge mode.

For the high-symmetry points d and f of the square lattice, assuming that the defect is symmetric enough so as to maintain the C_{4v} symmetry of the square lattice, the single acceptor mode is

$$\mathbf{H}_{A_2''}^{d,a1} = \hat{z} \left(\cos(\mathbf{k}_{M_1} \cdot \mathbf{r}^d) + \cos(\mathbf{k}_{M_2} \cdot \mathbf{r}^d) \right), \quad (1.37)$$

about point d , and

$$\mathbf{H}_{B_1''}^{f,a1} = \hat{z} \left(\cos(\mathbf{k}_{M_1} \cdot \mathbf{r}^f) - \cos(\mathbf{k}_{M_2} \cdot \mathbf{r}^f) \right), \quad (1.38)$$

about point f . The character of the representation S_e^{a1} of the M -point valence band edge mode under symmetry transformations C_{2v,σ_v} about point e is given in table 1.2. From its character, $S_e^{a1} = B_1$, the approximate acceptor mode of a defect centered about point e is

$$\mathbf{H}_{B_1''}^{e,a1} = \hat{z} \left(\sin(\mathbf{k}_{M_1} \cdot \mathbf{r}^e) - \sin(\mathbf{k}_{M_2} \cdot \mathbf{r}^e) \right). \quad (1.39)$$

For defects of reduced symmetry about points d and f we have the following compatibility relations:

$$\begin{array}{ccc} C_{4v} \rightarrow C_{2v,\sigma_v} & & C_{4v} \rightarrow C_{2v,\sigma_d} \\ \mathbf{H}_{A_2''}^{d,a1} \rightarrow \mathbf{H}_{A_2}^{d,a1} & \text{and} & \mathbf{H}_{A_2''}^{d,a1} \rightarrow \mathbf{H}_{A_2'}^{d,a1} \\ \mathbf{H}_{B_1''}^{f,a1} \rightarrow \mathbf{H}_{A_1}^{f,a1}, & & \mathbf{H}_{B_1''}^{f,a1} \rightarrow \mathbf{H}_{A_2'}^{f,a1}. \end{array} \quad (1.40)$$

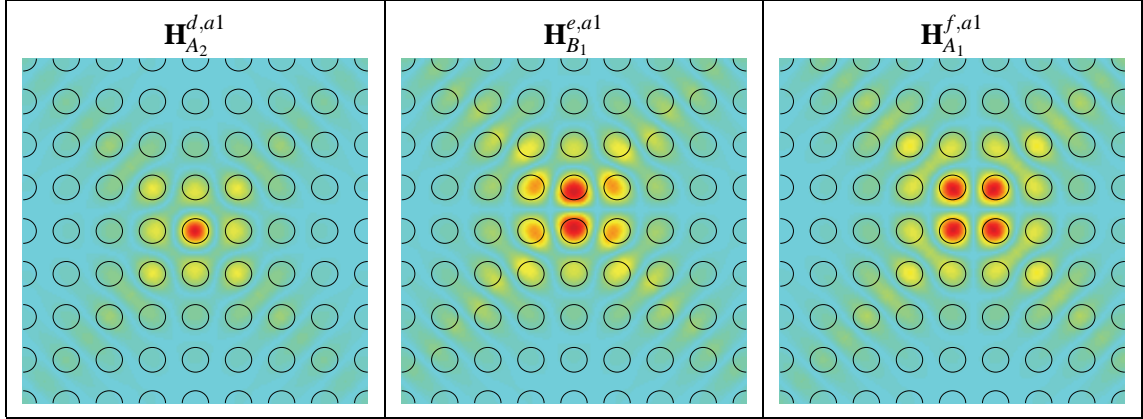


Figure 1.13: Magnetic field amplitude of the acceptor-type modes formed the valence band M -point modes of the square lattice.

Figure 1.13 shows the magnetic field patterns of the acceptor-type modes formed from the M -point of the IBZ of the square lattice for defects centered about points d , e , and f . Again, as for the donor modes, the modes are shown for the C_{2v,σ_v} symmetry basis.

1.1.4 Comparison with FDTD simulations

In order to establish the effectiveness of the above symmetry analysis of the modes of relatively localized defects within photonic crystals, we provide results of numerical calculations using the FDTD method. The FDTD simulation results provide information about the resonant frequency, radiation pattern, and modal loss of PC defect cavity resonant modes. The cavity studied in this section has been of particular relevance to the initial work on PC microcavity lasers performed by Painter et al. [3, 8].

The FDTD calculations (additional details provided in appendix B) were performed on a mesh with 20 points per lattice spacing. Excitation of the cavity modes was performed by an initial field (H_z) with a localized Gaussian profile, located in a position of low symmetry so as not to exclude any possible resonant modes. The even modes of the patterned slab waveguide were selected out by using an even mirror symmetry ($\sigma_h = +1$) in the middle of the slab waveguide. In order to choose a consistent mode basis (only important for degenerate modes), as well as to reduce computation time, a pair of vertical mirror planes (σ_x, σ_y) were used to filter out cavity modes according to their projection on the IRREPs of C_{2v} . Each cavity mode is thus labeled by the C_{2v} IRREP by which it transforms and an index corresponding to its energy (frequency) level.

The simplest cavity geometry that can be readily implemented consists of a single missing hole

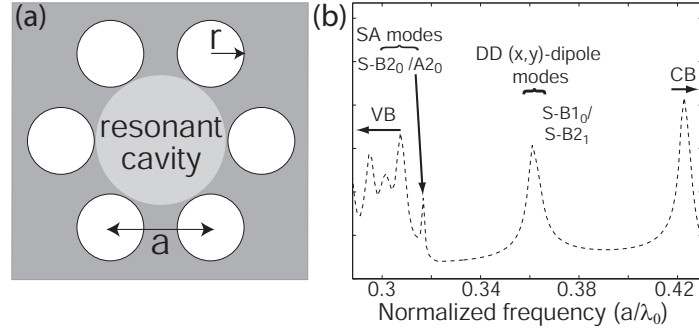


Figure 1.14: (a) S cavity (b) FDTD spectrum of a S -type defect cavity with $a = 515$ nm, $r/a = 0.36$ nominally, $n_{\text{slab}} = 3.4$, and $d/a = 0.409$.

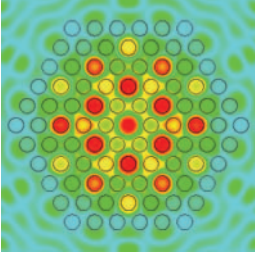
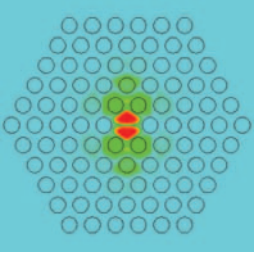
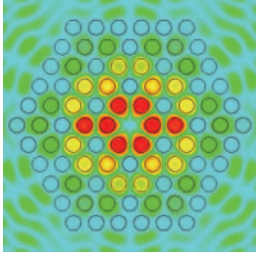
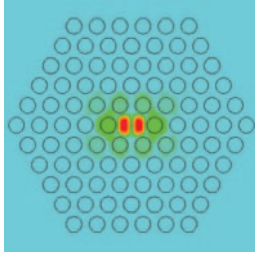
(schematically shown in fig. 1.14(a)). We will refer to this cavity as a symmetric or S cavity as it retains the full point group symmetry of the hexagonal lattice (C_{6v}). A FDTD-simulated spectrum of a defect cavity with a central missing hole and a linear grade in r/a (from the center outwards) of 0.38-0.34 is plotted in fig. 1.14(b) as a dashed line.² The spectrum is plotted versus normalized frequency, $\omega_n = a/\lambda_o$, where a is the lattice spacing and λ_o is the free-space wavelength. A normalized slab thickness, d/a , of 0.41 was used in the simulated structures to be consistent with the fabricated devices. To reduce computation time, the number of mirror periods (p) surrounding the central missing hole was limited to five in the simulations, save for the more extended modes for which cavities with eight periods were also simulated in order to more accurately estimate the modal losses present in the fabricated devices (see table 1.3).

In fig. 1.14, there appear to be two distinct resonance peaks within the guided mode bandgap of the TE-like modes. Performing a mode filter [7] using the C_{2v} mirror planes, we find that each resonance peak contains two different modes, yielding a total of four different localized modes whose magnetic field patterns within the mirror symmetry plane of the slab are shown in table 1.3. The two resonant modes (accidentally degenerate) associated with the peak near the valence band edge correspond to shallow acceptor (SA) modes which transform as the A_2'' and B_2'' IRREPs of C_{6v} ,³ and have the same dominant in-plane Fourier components as $\mathbf{H}_{A_2''}^{a1}$ and $\mathbf{H}_{B_2''}^{a1}$ of the symmetry analysis in section 1.1.2. The addition of these SA modes is a result of the linear grading in hole

²As a result of non-idealities in the fabrication process [95], the air holes near the center of the cavity are larger than those at the perimeter in the fabricated devices. A linear grading of the hole radius of 10% is quite common.

³Careful inspection of the FDTD generated magnetic field plot for these two modes shows that the mode patterns appear to have lower symmetry than that quoted in the text. This is a consequence of the way in which the modes were simulated, using vertical mirror planes to reduce the computation domain by a factor of four. Due to discretization of the computation grid, the mirror symmetry distorts the structure slightly, resulting in an asymmetry in the field pattern.

Table 1.3: Characteristics and magnetic field amplitude patterns of the resonant modes in a symmetric cavity with r/a linearly graded from 0.38 to 0.34 ($d/a = 0.409$, $n_{\text{slab}} = 3.4$, $p = 5$).

A2 $(-1, -1)$	B1 $(-1, +1)$	B2 $(+1, -1)$	
S-A2 ₀ 	S-B1 ₀ 	S-B2 ₀ 	S-B2 ₁ 
Label	Grp.	(σ_x, σ_y)	ω_n
S-A2 ₀ ($\mathbf{H}_{A_2'}^{a1}$)	SA	$(-, -)$	0.320
S-B1 ₀ ($\mathbf{H}_{E_{1,1}}^{d1}$)	DD	dipole (\mathbf{x})	0.361
S-B2 ₀ ($\mathbf{H}_{B_2'}^{a1}$)	SA	$(+, -)$	0.322
S-B2 ₁ ($\mathbf{H}_{E_{1,2}}^{d1}$)	DD	dipole (\mathbf{y})	0.360

radius, which forms a potential well for acceptor type modes. Of particular interest are the strongly localized pair of degenerate deep donor (DD) dipole-like modes near the center of the bandgap. From the plots of the electric field intensity of the x and y dipole modes shown in fig. 1.15(a)-(b), we see that the fundamental \mathbf{k} -components of the x and y dipole-like modes correspond nicely with the approximate field patterns predicted by the symmetry analysis (fig. 1.15(c)-(d)). Even the subtle difference in the in-plane radiation pattern of the x and y dipole modes as calculated numerically using FDTD is contained within the symmetry analysis as can be seen by the lack of a third standing wave component in the y -dipole ($\mathbf{H}_{E_{1,2}}^{d1}$) mode.

A list of properties of the two SA and two DD localized defect modes is given in table 1.3. The numerically calculated losses of each cavity mode are represented by effective in-plane and out-of-plane quality factors [7], Q_{\parallel} and Q_{\perp} , respectively. A detailed analysis of quality factors within PC cavities will be discussed in detail in the following chapter.

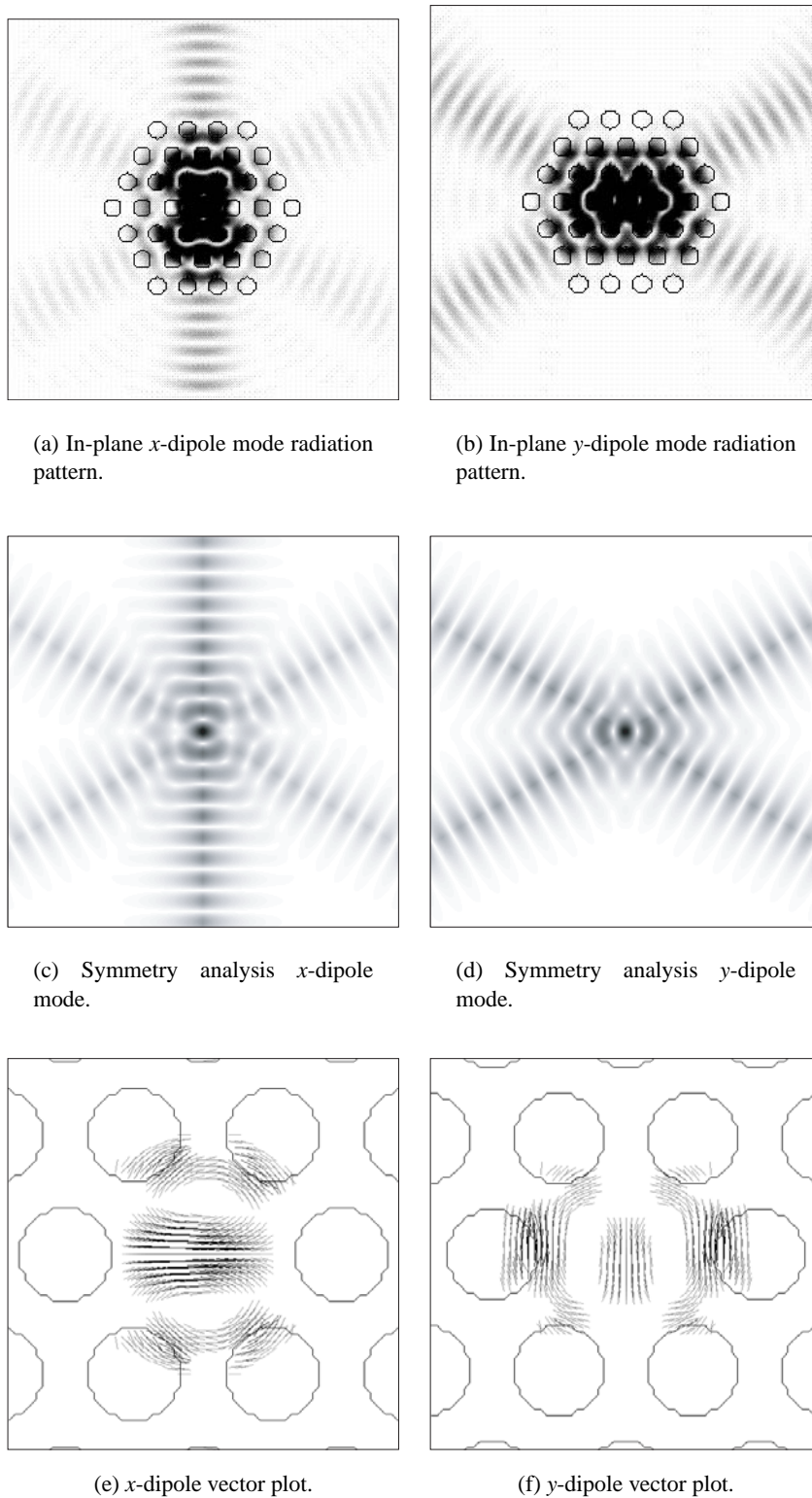


Figure 1.15: In-plane radiation losses (electric field amplitude saturated) of the x and y dipole mode (degenerate case) are shown in (a) and (b), respectively, as calculated by FDTD simulations. The electric field amplitude of the corresponding defect modes generated by the symmetry analysis are shown in (c) and (d) for comparison. In (e) and (f) the FDTD-generated vector plot of the electric field of the (x,y) -dipole modes in the middle of the slab waveguide are shown.

1.2 Wannier-like approach for describing localized modes in photonic crystals

1.2.1 Introduction

The work described in this section is largely based on ref. [25]. In analogy to the study of localized impurity states of electrons in periodic crystals [96, 97, 98, 99], we develop a Wannier-like wave equation to describe the envelope of resonant modes of localized perturbations within periodic dielectric structures. This has been done previously, in a more restrictive setting by Johnson et al. [100], and more recently in a general way by Charbonneau-Lefort et al. [101] and Istrate et al. [102] in the study of photonic crystal heterostructures. In these works, a wave equation for localized modes of non-uniform photonic crystals using an envelope approximation has been developed; however, in each case the envelope equation was formulated as a generalized Hermitian eigenvalue equation in terms of the electric field, and more importantly, only localized modes formed from non-degenerate satellite extrema were considered. In the analysis presented here we (i) consider the magnetic field and (ii) incorporate the mixing amongst the degenerate peaks or valleys of the orbit of \mathbf{k} in the bandstructure, resulting in a set of coupled Wannier-like equations describing a multi-envelope system. This allows us to more easily apply the envelope formalism to resonant cavity modes of PC slab waveguides, which in a two- or three-dimensional crystal mix Bloch modes near the degenerate satellite extrema of the orbit of \mathbf{k} . We also focus on the magnetic field as it can be approximately treated as a scalar for TE-like polarization modes of PC slabs⁴. From the shape and symmetry of the envelope of a localized resonant mode, and its relation to the underlying photonic bandstructure, one may better design features of planar 2D PC resonant cavities, such as in-plane and vertical emission, resonator-waveguide coupling, and the quality factor of resonant modes. In addition, the Wannier-like equation for localized defect modes more clearly and rigorously relates the curvature of the bandstructure to the formation of donor and acceptor modes for different types of local perturbations of a dielectric lattice.

This section is organized as follows. In section 1.2.2 we derive a set of coupled Wannier-like equations for the envelope functions of localized TE-like states in planar 2D PC structures, where as predicted by the Wannier theorem, the underlying bandstructure of the periodic dielectric structure gives rise to an effective mass tensor. We also derive an approximate form for the effective potential

⁴It should be noted that the envelope is always a scalar field, regardless of the vector nature of the electric or magnetic field.

in the Wannier envelope equation in terms of the local perturbation to the dielectric lattice. In section 1.2.3 we use the approximate symmetry basis for the TE-like Bloch modes at the valence and conduction band edge of the first-order bandgap in a 2D photonic crystal consisting of a hexagonal array of air holes derived in the previous section to obtain approximate relations for the effective mass tensor of the Wannier equation. In conjunction with the symmetry analysis, which determines the mixing amongst the degenerate satellite extrema, we find an approximate form for the localized donor and acceptor modes of a hexagonal lattice with a parabolically graded filling fraction. For comparison, FDTD calculations of the acceptor and donor modes of such a defect cavity are also presented.

1.2.2 Wannier theorem for photons in periodic dielectric structures

In studying the localized electronic states associated with impurities within a crystalline material, it is often helpful to transform Schrödinger's equation into Fourier space, simplify the set of coupled equations through the limited Fourier decomposition of the perturbing potential, and then transform back to real-space coordinates, where a wave equation for the envelope of the localized states is generated. The Wannier theorem [103] captures the essence of this procedure in using the underlying energy-(crystal)momentum dispersion generated by the periodic Coulombic potential of the crystal in a spatially coarse-grained theory of electron dynamics. One application of the Wannier theorem is in the calculation of bound electronic states of crystal impurities [96, 99, 97, 98, 104]. The basic form of the Wannier equation for the envelope of impurity states is

$$\left((E - E_n(\hbar^{-1}\hat{\mathbf{p}})) + \Delta V(\mathbf{r}) \right) \Gamma(\mathbf{r}) = 0, \quad (1.41)$$

where $E_n(\hbar^{-1}\hat{\mathbf{p}})$ is the energy-(crystal)momentum dispersion relation of the n th energy band with wavevector \mathbf{k} replaced by the canonical momentum operator $\hat{\mathbf{p}} = -i\hbar\nabla$, $\Delta V(\mathbf{r})$ is the impurity potential, and $\Gamma(\mathbf{r})$ is the envelope function describing the localized electronic state.

We would like to find a similar Wannier-like equation for the envelope of localized photon states in periodic dielectric lattices. Of particular interest are the localized resonant modes of planar 2D PCs formed in optically thin dielectric slabs (see fig. 1.1). The fundamental TE-like even modes and TM-like odd modes of a symmetric 2D patterned dielectric slab waveguide can be approximated by scalar fields. In what follows we shall focus on the TE-like modes (as discussed in ref. [25], a

similar theory may also be derived for the TM-like modes of the PC slab).

We begin with Maxwell's equations in a (lossless) dielectric medium free of currents and free charge,

$$\begin{aligned}
\nabla \times \mathbf{E} &= -i\omega\mu_0\mathbf{H}, \\
\nabla \times \mathbf{H} &= +i\omega n^2\varepsilon_0\mathbf{E}, \\
\nabla \cdot (n^2\varepsilon_0\mathbf{E}) &= 0, \\
\nabla \cdot \mu_0\mathbf{H} &= 0,
\end{aligned} \tag{1.42}$$

where \mathbf{E} and \mathbf{H} are the harmonic complex electric and magnetic fields, respectively, with time dependence $e^{+i\omega t}$ (the physical fields are found by taking the real part of the complex fields). The velocity of light in vacuum is represented by c , and we have assumed that the material is non-magnetic ($\mu = \mu_0$). We also assume here that the dielectric function does not depend on spatial or temporal frequency, $\varepsilon(\omega, \mathbf{k}, \mathbf{r}) = \varepsilon_0 n^2(\mathbf{r})$. From the above Maxwell relations, a wave equation for both the electric and magnetic fields can be generated:

$$\eta(\mathbf{r}) \left(\nabla \times \nabla \times \mathbf{E} \right) = \left(\frac{\omega}{c} \right)^2 \mathbf{E}, \tag{1.43}$$

$$\nabla \times \left(\eta(\mathbf{r}) \nabla \times \mathbf{H} \right) = \left(\frac{\omega}{c} \right)^2 \mathbf{H}, \tag{1.44}$$

where $\eta(\mathbf{r}) \equiv 1/n^2(\mathbf{r})$.

As we have discussed in the previous section, we separate modes into TE and TM polarizations, keeping in mind that this separation is only truly valid for purely 2D structures (for slab waveguides, the modes are only approximately TE and TM in nature). For TE modes the magnetic field is described by a scalar field, $\mathbf{H} = \hat{z}H_d$ (where the subscript d stands for “defect mode”). As we have assumed that the refractive index does not vary (or the variation can be approximately neglected) in the \hat{z} -direction, $\partial_z \eta(\mathbf{r}) = 0$. The Hermitian eigenvalue equation which results from equation (1.44) and $\nabla \cdot \mathbf{H} = 0$ is (in the 2D case we only consider variations with respect to the in-plane coordinates, $\nabla \equiv \nabla_{\perp}$),

$$\hat{L}_H^{\text{TE}} H_d = \Lambda_d H_d, \quad (1.45)$$

with the TE eigenoperator given by,

$$\hat{L}_H^{\text{TE}} = -(\nabla\eta) \cdot \nabla - \eta \nabla^2. \quad (1.46)$$

The form of TE eigenoperator is easily obtained from equation (1.44) by using standard vector calculus identities as found in ref. [93], for example. The eigenvalue, Λ_d , is related to the square of the frequency of the mode, $\Lambda_d = (\omega_d/c)^2$. $\eta = \eta_o + \Delta\eta$, where η_o is given by the inverse of the square of the refractive index of the unperturbed photonic crystal, $1/n_{2D}^2(\mathbf{r})$, and $\Delta\eta$ represents the localized perturbation to $1/n_{2D}^2(\mathbf{r})$. The eigenoperator \hat{L}_H (we drop the TE superscript from here on) can be separated into an unperturbed photonic crystal part, $\hat{L}_{H,o} = -\nabla(\eta_o) \cdot \nabla - \eta_o \nabla^2$, and a perturbation part due to the defect, $\hat{L}'_H = -\nabla(\Delta\eta) \cdot \nabla - \Delta\eta \nabla^2$.

The (2D approximate) modes of the perfect crystal are eigenmodes of $\hat{L}_{H,o}$,

$$\hat{L}_{H,o} H_{l,\mathbf{k}} = \Lambda_{l,\mathbf{k}} H_{l,\mathbf{k}}, \quad (1.47)$$

where l labels the band index and \mathbf{k} labels the in-plane crystal momentum. As the $H_{l,\mathbf{k}}$ are Bloch waves they can be written as

$$H_{l,\mathbf{k}} = \frac{1}{L} h_{l,\mathbf{k}}(\mathbf{r}) e^{i\mathbf{k}\cdot\mathbf{r}}, \quad (1.48)$$

with L^2 equal to the area of the 2D photonic crystal and the set of periodic functions, $h_{l,\mathbf{k}}(\mathbf{r})$, at crystal momentum \mathbf{k} , satisfying their own set of orthogonality relations (normalized over the lattice unit cell v),

$$\langle h_{l',\mathbf{k}} | h_{l,\mathbf{k}} \rangle_v \equiv \frac{1}{v} \int_v d^2r h_{l',\mathbf{k}}^* h_{l,\mathbf{k}} = \delta_{l',l}. \quad (1.49)$$

In forming a defect state by perturbing the lattice in a localized region of space, the Bloch modes in proximity to the degenerate satellite extrema of a band edge, the $\{\mathbf{k}_i; i = 1, 2, \dots, M\}$ points of the $\star\mathbf{k}$ (from here on, the $\star\mathbf{k}$ refers implicitly to the orbit of this band edge), are most strongly coupled together [98]:

$$H_d(\mathbf{r}) = \sum_i c_i \sum_{\mathbf{k}} \tilde{\Gamma}_i(\mathbf{k} - \mathbf{k}_i) \frac{1}{L} h_{l,\mathbf{k}} e^{i\mathbf{k}\cdot\mathbf{r}}, \quad (1.50)$$

The $\tilde{\Gamma}_i$ are a set of Fourier space envelope functions, which in the spirit of the effective mass theory have amplitudes localized around $\mathbf{k} = \mathbf{k}_i$. Note that throughout this analysis the band of interest at the band edge is considered to be non-degenerate and we neglect *inter*-band mixing [98].

Assuming that the $h_{l,\mathbf{k}}$ do not vary significantly (using a similar argument as in ref. [97]) over the range of each Fourier space envelope function,

$$H_d(\mathbf{r}) \approx \sum_i c_i \frac{1}{L} h_{l,\mathbf{k}_i} e^{i\mathbf{k}_i\cdot\mathbf{r}} \left(\sum_{\Delta\mathbf{k}} \tilde{\Gamma}_i(\Delta\mathbf{k}) e^{i\Delta\mathbf{k}\cdot\mathbf{r}} \right), \quad (1.51)$$

where $\Delta\mathbf{k} \equiv \mathbf{k} - \mathbf{k}_i$. Writing the envelope functions in real space,

$$\Gamma_i(\mathbf{r}) = \sum_{\Delta\mathbf{k}} \tilde{\Gamma}_i(\Delta\mathbf{k}) e^{i\Delta\mathbf{k}\cdot\mathbf{r}}, \quad (1.52)$$

allows us to rewrite equation (1.51) as,

$$H_d(\mathbf{r}) \approx \sum_i c_i \frac{1}{L} h_{l,\mathbf{k}_i} e^{i\mathbf{k}_i\cdot\mathbf{r}} \Gamma_i(\mathbf{r}), \quad (1.53)$$

It is in this way that the real space envelope of localized defect modes can be interpreted in the Fourier domain [97] as a result of the *intra*-band mixing of the unperturbed Bloch modes of the crystal.

Returning to equation (1.45), we now proceed to find an eigenvalue equation for the envelope functions. Multiplying both sides of equation (1.45) by $H_{l',\mathbf{k}'}$, where \mathbf{k}' is chosen in a neighborhood of \mathbf{k}_i , and integrating over the in-plane spatial coordinates gives,

$$\sum_j c_j \sum_{\mathbf{k}} \tilde{\Gamma}_j(\mathbf{k} - \mathbf{k}_j) \langle H_{l',\mathbf{k}'} | (\Lambda_d - \Lambda_{l,\mathbf{k}} - \hat{L}'_H) H_{l,\mathbf{k}} \rangle = 0. \quad (1.54)$$

We rewrite \mathbf{r} as $\mathbf{R}_i + \mathbf{r}$, where \mathbf{R}_i gives the center of the i^{th} unit cell and \mathbf{r} is now confined to the interior of the unit cell. Using the orthonormality of the Bloch waves and the normalization of their periodic parts described in equation (1.49),

$$\begin{aligned} \langle H_{l',\mathbf{k}'} | (\Lambda_d - \Lambda_{l,\mathbf{k}}) H_{l,\mathbf{k}} \rangle &= (\Lambda_d - \Lambda_{l,\mathbf{k}}) \frac{1}{L^2} \sum_{i=1}^N e^{i(\mathbf{k}-\mathbf{k}') \cdot \mathbf{R}_i} \int_{\mathcal{V}} d^2r h_{l',\mathbf{k}'}^* h_{l,\mathbf{k}} e^{i(\mathbf{k}-\mathbf{k}') \cdot \mathbf{r}} \\ &= (\Lambda_d - \Lambda_{l',\mathbf{k}'}) \delta_{l',l} \delta_{\mathbf{k}',\mathbf{k}}. \end{aligned} \quad (1.55)$$

Note that a reciprocal lattice vector was not included in $\delta_{\mathbf{k}',\mathbf{k}}$ as both \mathbf{k}' and \mathbf{k} (through the localized nature of the $\tilde{\Gamma}_i$) are assumed to lie within a neighborhood of one of the wavevectors comprising the $\star\mathbf{k}$, which by definition are not linked by a reciprocal lattice vector. Equation (1.54) then becomes

$$\begin{aligned} c_i (\Lambda_d - \Lambda_{l,\mathbf{k}'}) \tilde{\Gamma}_i(\mathbf{k}' - \mathbf{k}_i) \\ - \sum_j c_j \sum_{\mathbf{k}} \langle H_{l',\mathbf{k}'} | \hat{L}'_H H_{l,\mathbf{k}} \rangle \tilde{\Gamma}_j(\mathbf{k} - \mathbf{k}_j) = 0. \end{aligned} \quad (1.56)$$

Fourier expanding the defect perturbation in reciprocal space,

$$\Delta\eta(\mathbf{r}) = \sum_{\mathbf{k}''} \tilde{\Delta}\eta_{\mathbf{k}''} e^{i\mathbf{k}'' \cdot \mathbf{r}}, \quad (1.57)$$

we can write the mode-mixing term $\langle H_{l',\mathbf{k}'} | \hat{L}'_H H_{l,\mathbf{k}} \rangle$ in equation (1.56) as:

$$\begin{aligned} \langle H_{l',\mathbf{k}'} | \hat{L}'_H H_{l,\mathbf{k}} \rangle &= - \sum_{\mathbf{k}''} \left(\sum_{i=1}^N e^{i(\mathbf{k}+\mathbf{k}''-\mathbf{k}') \cdot \mathbf{R}_i} \frac{\tilde{\Delta}\eta_{\mathbf{k}''}}{L^2} \int_{\mathcal{V}} d^2r e^{i(\mathbf{k}+\mathbf{k}''-\mathbf{k}') \cdot \mathbf{r}} h_{l',\mathbf{k}'}^* \left(i\mathbf{k}'' \cdot (\nabla + i\mathbf{k}) \right. \right. \\ &\quad \left. \left. + \nabla^2 + 2i\mathbf{k} \cdot \nabla - |\mathbf{k}|^2 \right) h_{l,\mathbf{k}} \right) \\ &= \sum_{\mathbf{G}} \sum_{\mathbf{k}''} \left(\tilde{\Delta}\eta_{\mathbf{k}''} K_{l',l}(\mathbf{k}', \mathbf{k}, \mathbf{G}) + \tilde{\Delta}\eta_{\mathbf{k}''}(i\mathbf{k}'') \cdot \mathbf{L}_{l',l}(\mathbf{k}', \mathbf{k}, \mathbf{G}) \right) \delta_{\mathbf{k}'-\mathbf{k}''+\mathbf{G},\mathbf{k}}, \end{aligned} \quad (1.58)$$

where the \mathbf{G} are reciprocal lattice vectors, and we have defined scalar and vector coupling matrix elements as

$$\begin{aligned} K_{l',l}(\mathbf{k}', \mathbf{k}, \mathbf{G}) &= -\frac{1}{v} \int_v d^2r e^{i\mathbf{G}\cdot\mathbf{r}} h_{l',\mathbf{k}'}^* (\nabla^2 + 2i\mathbf{k}\cdot\nabla - |\mathbf{k}|^2) h_{l,\mathbf{k}} \\ &\equiv -\langle h_{l',\mathbf{k}'} | e^{i\mathbf{G}\cdot\mathbf{r}} (\nabla^2 + 2i\mathbf{k}\cdot\nabla - |\mathbf{k}|^2) | h_{l,\mathbf{k}} \rangle_v, \end{aligned} \quad (1.59)$$

and

$$\begin{aligned} \mathbf{L}_{l',l}(\mathbf{k}', \mathbf{k}, \mathbf{G}) &= -\frac{1}{v} \int_v d^2r e^{i\mathbf{G}\cdot\mathbf{r}} h_{l',\mathbf{k}'}^* (\nabla + i\mathbf{k}) h_{l,\mathbf{k}} \\ &\equiv -\langle h_{l',\mathbf{k}'} | e^{i\mathbf{G}\cdot\mathbf{r}} (\nabla + i\mathbf{k}) | h_{l,\mathbf{k}} \rangle_v. \end{aligned} \quad (1.60)$$

Substituting equation (1.58) into equation (1.56) while keeping only terms that mix states within the l th band results in the following Fourier space representation of the magnetic field master equation:

$$\begin{aligned} c_i(\Lambda_d - \Lambda_{l,\mathbf{k}'}) \widetilde{\Gamma}_i(\mathbf{k}' - \mathbf{k}_i) - \sum_{\mathbf{G}} \sum_j c_j \sum_{\mathbf{k}''} \left(\left(\widetilde{\Delta\eta}_{\mathbf{k}''} K_{l,l}(\mathbf{k}', \mathbf{k}' - \mathbf{k}'' + \mathbf{G}, \mathbf{G}) \right. \right. \\ \left. \left. + \widetilde{\Delta\eta}_{\mathbf{k}''}(i\mathbf{k}'') \cdot \mathbf{L}_{l,l}(\mathbf{k}', \mathbf{k}' - \mathbf{k}'' + \mathbf{G}, \mathbf{G}) \right) \widetilde{\Gamma}_j((\mathbf{k}' - \mathbf{k}'' + \mathbf{G}) - \mathbf{k}_j) \right) = 0. \end{aligned} \quad (1.61)$$

For defect perturbations which are localized in \mathbf{k} -space as well as in real-space, the strongest mixing terms will be those with \mathbf{k}'' nearest the origin. As such, a further simplification can be made by including only those reciprocal lattice vectors \mathbf{G} which minimize the magnitude of \mathbf{k}'' in coupling the different neighborhoods of the $\star\mathbf{k}$ (satellite extrema). The local mixing of states within the neighborhood of each \mathbf{k}_i will thus be dominated by the Fourier components of $\widetilde{\Delta\eta}$ about the origin with $\mathbf{G} = 0$. Similarly, the mixing between neighborhoods of \mathbf{k}_i and \mathbf{k}_j , where $i \neq j$, will be dominated by a single \mathbf{G} which minimizes the magnitude of the vector $\mathbf{G} - (\mathbf{k}_j - \mathbf{k}_i)$. Writing this reciprocal lattice vector as $\mathbf{G}_{j,i}$ and only including the dominant coupling terms in equation (1.61) collapses the sum over \mathbf{G} and yields,

$$\begin{aligned}
& c_i \left((\Lambda_d - \Lambda_{l,\mathbf{k}'}) \tilde{\Gamma}_i(\mathbf{k}' - \mathbf{k}_i) - \sum_{\mathbf{k}''} \left(\tilde{\Delta}\eta_{\mathbf{k}''} K_{l,l}(\mathbf{k}_i, \mathbf{k}_i, \mathbf{0}) + \tilde{\Delta}\eta_{\mathbf{k}''}(i\mathbf{k}'') \cdot \mathbf{L}_{l,l}(\mathbf{k}_i, \mathbf{k}_i, \mathbf{0}) \right) \right. \\
& \left. \tilde{\Gamma}_i((\mathbf{k}' - \mathbf{k}'') - \mathbf{k}_i) \right) - \sum_{i \neq j} c_j \sum_{\mathbf{k}''} \left(\left(\tilde{\Delta}\eta_{\mathbf{k}''} K_{l,l}(\mathbf{k}_i, \mathbf{k}_j, \mathbf{G}_{j,i}) + \tilde{\Delta}\eta_{\mathbf{k}''}(i\mathbf{k}'') \cdot \mathbf{L}_{l,l}(\mathbf{k}_i, \mathbf{k}_j, \mathbf{G}_{j,i}) \right) \right. \\
& \left. \tilde{\Gamma}_j((\mathbf{k}' - (\mathbf{k}'' - \mathbf{G}_{j,i})) - \mathbf{k}_j) \right) = 0,
\end{aligned} \quad (1.62)$$

where we have neglected the variation of $K_{l,l}$ and $\mathbf{L}_{l,l}$ within the local neighborhoods of the $\mathbf{k}_i \in \star\mathbf{k}$.

Implicit in the derivation of equation (1.62) is that the $\tilde{\Gamma}_i$ are localized around the \mathbf{k}_i in reciprocal space. In order to make this explicit (which will be necessary when transforming back to real-space coordinates) we expand $\Lambda_{l,\mathbf{k}'}$ in the vicinity of each \mathbf{k}_i ,

$$\Lambda_{l,\mathbf{k}'} \approx (\Lambda_{l,o} + \Lambda'_{l,i}(\Delta\mathbf{k})) + O(\Delta k^3), \quad (1.63)$$

where $\Lambda_{l,o}$ is the top(bottom) of the band edge, $\Delta\mathbf{k} = \mathbf{k}' - \mathbf{k}_i$, and $\Lambda'_{l,i}$ only contains terms up to second-order in elements of $\Delta\mathbf{k}$ [98]. In the case of those \mathbf{k}_i located at an extrema of a given (non-degenerate) band the resulting dispersion relation may be written in the form, $\Lambda'_{l,i}(\Delta\mathbf{k}) = \Delta\mathbf{k} \cdot \mathbf{M}_{l,*}^{-1} \cdot \Delta\mathbf{k}$, where the matrix $\mathbf{M}_{l,*}$ is an effective mass tensor defined by the curvature of the band. Substituting equation (1.63) into equation (1.62) gives,

$$\begin{aligned}
& c_i \left((\Delta\Lambda_d - \Lambda'_{l,i}(\Delta\mathbf{k})) \tilde{\Gamma}_i(\Delta\mathbf{k}) - \sum_{\mathbf{k}''} \left(\tilde{\Delta}\eta_{\mathbf{k}''} K_{l,l}(\mathbf{k}_i, \mathbf{k}_i, \mathbf{0}) + \tilde{\Delta}\eta_{\mathbf{k}''}(i\mathbf{k}'') \cdot \mathbf{L}_{l,l}(\mathbf{k}_i, \mathbf{k}_i, \mathbf{0}) \right) \right. \\
& \left. \tilde{\Gamma}_i(\Delta\mathbf{k} - \mathbf{k}'') \right) - \sum_{i \neq j} c_j \sum_{\mathbf{k}''} \left(\left(\tilde{\Delta}\eta_{\mathbf{k}''} K_{l,l}(\mathbf{k}_i, \mathbf{k}_j, \mathbf{G}_{j,i}) + \tilde{\Delta}\eta_{\mathbf{k}''}(i\mathbf{k}'') \cdot \mathbf{L}_{l,l}(\mathbf{k}_i, \mathbf{k}_j, \mathbf{G}_{j,i}) \right) \right. \\
& \left. \tilde{\Gamma}_j((\Delta\mathbf{k} + \mathbf{G}_{j,i} - \Delta\mathbf{k}_{j,i}) - \mathbf{k}'') \right) = 0,
\end{aligned} \quad (1.64)$$

where $\Delta\Lambda_d = \Lambda_d - \Lambda_{l,o}$ is the eigenvalue referenced to the top(bottom) of the band edge, and $\Delta\mathbf{k}_{j,i} \equiv \mathbf{k}_j - \mathbf{k}_i$.

Equation (1.64) is the Fourier space representation of an approximate master equation for the localized magnetic field envelope functions of defect states. Transforming back to real space results in a set of coupled Wannier-like equations,

$$c_i \left((\Delta\Lambda_d - \Lambda'_{l,i}(\hbar^{-1}\hat{\mathbf{p}})) - \Delta\eta'_{i,i}(\mathbf{r}) \right) \Gamma_i(\mathbf{r}) - \sum_{i \neq j} c_j \left(e^{-i(\mathbf{G}_{j,i} - \Delta\mathbf{k}_{j,i}) \cdot \mathbf{r}} \Delta\eta'_{j,i}(\mathbf{r}) \right) \Gamma_j(\mathbf{r}) = 0, \quad (1.65)$$

$$\Delta\eta'_{j,i}(\mathbf{r}) = \Delta\eta(\mathbf{r}) K_{l,l}(\mathbf{k}_i, \mathbf{k}_j, \mathbf{G}_{j,i}) + \nabla(\Delta\eta(\mathbf{r})) \cdot \mathbf{L}_{l,l}(\mathbf{k}_i, \mathbf{k}_j, \mathbf{G}_{j,i}), \quad (1.66)$$

where $\hat{\mathbf{p}} = -i\hbar\nabla$ as in quantum mechanics, and $\Delta\eta'_{j,i}(\mathbf{r})$ is an effective perturbation potential.

Assuming that the amplitude of the relatively large Fourier components of $\Delta\eta(\mathbf{r})$ associated with mixing of states between neighborhoods of *different* satellite points of the $\star\mathbf{k}$ are much smaller than the amplitude of the small Fourier components which mix states within a given neighborhood of a point of the $\star\mathbf{k}$, we can treat the *inter- \mathbf{k}_i* mixing as a perturbation to the envelope functions formed from the local \mathbf{k} -space mixing [104]. This allows us to write an independent Wannier-like equation for each of the $\Gamma_i(\mathbf{r})$ envelope functions,

$$\left((\Delta\Lambda_d - \Lambda'_{l,i}(\hbar^{-1}\hat{\mathbf{p}})) - \Delta\eta'_{i,i}(\mathbf{r}) \right) \Gamma_i(\mathbf{r}) = 0. \quad (1.67)$$

Of most importance for the types of resonant cavities studied here are the ground state solutions to equation (1.67). This is due to the relatively localized nature of the defect regions. For delocalized defect regions extending over many lattice periods a more extensive set of envelope functions, including higher order functions with added nodes and antinodes must be included. Choice of such a set of envelope functions will depend on the geometry of the boundary of the defect [105]. For the present work then, we take $\Gamma_i(\mathbf{r})$ equal to the ground state envelope, $\Gamma_{i,o}(\mathbf{r})$.

As the ground state of a system is in general invariant under the symmetries of the Hamiltonian of that system [106, 104], the ground state envelope function should transform as the identity of the point group of the Wannier-like equation given in equation (1.67). The spatial symmetries of equation (1.67) are those of $\Lambda'_{l,i}(\hbar^{-1}\hat{\mathbf{p}})$ and $\Delta\eta'_{i,i}(\mathbf{r})$. As discussed in ref. [24], it then follows that the point symmetries of the Wannier-like equation for the ground state envelope functions are given by $G' \cap G'_{\mathbf{k}_i}$, where G' is the point group of the defect perturbation (independent of the crystal lattice) and $G'_{\mathbf{k}_i}$ is the point group isomorphic to the group of the wavevector (of the underlying Bravais lattice) at the point \mathbf{k}_i in the IBZ. With this knowledge the coefficients c_i of the defect state

in equation (1.53) can then be determined using symmetry arguments.

1.2.3 Envelope function calculation

We will consider two examples of how the Wannier-like equation of the previous section can be used to calculate an approximate envelope function for a localized photon state in a hexagonal lattice photonic crystal. The first example is a localized donor-type mode formed at the band edge occurring at the X -point of the reciprocal lattice where the bandstructure (fig. 1.2(a)) has a local minimum and is given by a simple paraboloid in a neighborhood of the X -point. The second example is that of a localized acceptor-type mode formed from the J -point where the bandstructure has a local maximum.

1.2.3.1 Donor modes at the X -point

We begin by recalling equations 1.5 and 1.6 of section 1.1.2.1, which give an approximate representation for the band edge modes at the X -point of the hexagonal lattice. In particular, we found

$$VB_X^a = \begin{pmatrix} v_{X_1} \\ v_{X_2} \\ v_{X_3} \end{pmatrix} = \hat{z} \begin{pmatrix} \cos(\mathbf{k}_{X_1} \cdot \mathbf{r}^a) \\ \cos(\mathbf{k}_{X_2} \cdot \mathbf{r}^a) \\ \cos(\mathbf{k}_{X_3} \cdot \mathbf{r}^a) \end{pmatrix}, \quad (1.68)$$

as an approximate form for the X -point valence band modes, and

$$CB_X^a = \begin{pmatrix} c_{X_1} \\ c_{X_2} \\ c_{X_3} \end{pmatrix} = \hat{z} \begin{pmatrix} \sin(\mathbf{k}_{X_1} \cdot \mathbf{r}^a) \\ \sin(\mathbf{k}_{X_2} \cdot \mathbf{r}^a) \\ \sin(\mathbf{k}_{X_3} \cdot \mathbf{r}^a) \end{pmatrix}. \quad (1.69)$$

as an approximate form for the X -point conduction band modes. Separating the plane wave and periodic parts of the above Bloch modes allows us to write,

$$\begin{aligned} v_{X_i} &= \frac{\hat{z}}{2}(1 + e^{-i2\mathbf{k}_{X_i} \cdot \mathbf{r}^a})e^{i\mathbf{k}_{X_i} \cdot \mathbf{r}^a}, \\ c_{X_i} &= \frac{\hat{z}}{i2}(1 - e^{-i2\mathbf{k}_{X_i} \cdot \mathbf{r}^a})e^{i\mathbf{k}_{X_i} \cdot \mathbf{r}^a}, \end{aligned} \quad (1.70)$$

with normalized periodic functions given by

$$\begin{aligned} h_{v,\mathbf{k}_{X_i}} &= (1/\sqrt{2})(1 + e^{-i2\mathbf{k}_{X_i} \cdot \mathbf{r}^a}), \\ h_{c,\mathbf{k}_{X_i}} &= (1/i\sqrt{2})(1 - e^{-i2\mathbf{k}_{X_i} \cdot \mathbf{r}^a}). \end{aligned} \quad (1.71)$$

We now use the above set of modes to calculate the local dispersion of the conduction band at the X -point. The Hermitian operator acting on the space of periodic functions at point \mathbf{k} in the reciprocal lattice, for the quasi-2D case studied here, is

$$\hat{L}_{H,\mathbf{k}} = -\nabla(\eta_o) \cdot (i\mathbf{k} + \nabla) + \eta_o(|\mathbf{k}|^2 - 2i\mathbf{k} \cdot \nabla - \nabla^2), \quad (1.72)$$

with associated eigenvalue equation given by,

$$\hat{L}_{H,\mathbf{k}} h_{l,\mathbf{k}} = \Lambda_{l,\mathbf{k}} h_{l,\mathbf{k}}. \quad (1.73)$$

As in “ $\mathbf{k} \cdot \hat{\mathbf{p}}$ ” theory for Bloch electrons in crystalline materials, we expand $\hat{L}_{H,\mathbf{k}}$ about point \mathbf{k}_o ,

$$\hat{L}_{H,\mathbf{k}} = \hat{L}_{H,\mathbf{k}_o} + \hat{L}'_{H,\Delta\mathbf{k}}, \quad (1.74)$$

with

$$\hat{L}'_{H,\Delta\mathbf{k}} \equiv \eta_o |\Delta\mathbf{k}|^2 + \Delta\mathbf{k} \cdot (-i\nabla(\eta_o) + 2\eta_o \mathbf{k}_o - 2i\eta_o \nabla). \quad (1.75)$$

Treating $\hat{L}'_{H,\Delta\mathbf{k}}$ as a perturbation to \hat{L}_{H,\mathbf{k}_o} , and expanding $h_{l,\mathbf{k}}$ in terms of the h_{l,\mathbf{k}_o} ,⁵ gives to second

⁵As discussed in ref. [107], the h_{l,\mathbf{k}_o} are not complete in the space of lattice periodic functions due to the divergenceless

order in elements of $\Delta\mathbf{k}$,

$$\begin{aligned} \Lambda_{l,\mathbf{k}\sim\mathbf{k}_o} &= \Lambda_{l,\mathbf{k}_o} + \Delta\mathbf{k} \cdot \langle h_{l,\mathbf{k}_o} | (-i\nabla(\eta_o) + 2\eta_o\mathbf{k}_o - 2i\eta_o\nabla) | h_{l,\mathbf{k}_o} \rangle_v + |\Delta\mathbf{k}|^2 \langle h_{l,\mathbf{k}_o} | \eta_o | h_{l,\mathbf{k}_o} \rangle_v \\ &+ \sum_{l' \neq l} \frac{|\Delta\mathbf{k} \cdot \langle h_{l',\mathbf{k}_o} | (-i\nabla(\eta_o) + 2\eta_o\mathbf{k}_o - 2i\eta_o\nabla) | h_{l,\mathbf{k}_o} \rangle_v|^2}{(\Lambda_{l,\mathbf{k}_o} - \Lambda_{l',\mathbf{k}_o})}. \end{aligned} \quad (1.76)$$

If \mathbf{k}_o corresponds to an extremal point within the bandstructure, then the linear $\Delta\mathbf{k}$ terms in equation (1.76) are identically zero. One can check that for the X -point conduction and valence band modes of equation (1.70), this is indeed the case. Substituting the periodic functions of the conduction and valence band modes of equation (1.71) into equation (1.76) gives the local X -point bandstructure of the conduction band as:

$$\begin{aligned} \Lambda_{c,\mathbf{k}\sim\mathbf{k}_{X_i}} &= \Lambda_{c,\mathbf{k}_{X_i}} + |\Delta\mathbf{k}|^2 \langle h_{c,\mathbf{k}_{X_i}} | \eta_o | h_{c,\mathbf{k}_{X_i}} \rangle_v \\ &+ \frac{|\Delta\mathbf{k} \cdot \langle h_{v,\mathbf{k}_{X_i}} | (-i\nabla(\eta_o) + 2\eta_o\mathbf{k}_{X_i} - 2i\eta_o\nabla) | h_{c,\mathbf{k}_{X_i}} \rangle_v|^2}{\Delta\Lambda_X}, \end{aligned} \quad (1.77)$$

where $\Delta\Lambda_X \equiv (\Lambda_{c,\mathbf{k}_X} - \Lambda_{v,\mathbf{k}_X})$.

Fourier expanding η_o ,

$$\eta_o = \sum_{\mathbf{G}} \tilde{\eta}_{o,\mathbf{G}} e^{i\mathbf{G}\cdot\mathbf{r}^a}, \quad (1.78)$$

allows the bandstructure to be evaluated in terms of the Fourier coefficients of the dielectric PC. Since η_o is a lattice periodic *real* function, \mathbf{G} are reciprocal lattice vectors and $\tilde{\eta}_{o,\mathbf{G}} = (\tilde{\eta}_{o,-\mathbf{G}})^*$. With the origin located at point a of the lattice (see fig. 1.2(a)), the hexagonal PC has C_{6v} symmetry. As a result the Fourier coefficients of the hexagonal lattice are all real (inversion symmetry of the lattice), and $\tilde{\eta}_{o,2\mathbf{k}_{X_i}} = \tilde{\eta}_{o,2\mathbf{k}_{X_j}}$, for all $\mathbf{k}_{X_i}, \mathbf{k}_{X_j} \in \star\mathbf{k}$. Also, as point a lies within the center of an air hole, the fundamental Fourier coefficients of the lattice, $\tilde{\eta}_{o,2\mathbf{k}_{X_i}}$, must be positive. Substituting equation (1.78) into equation (1.77) gives,

nature of the magnetic field. In order to form a complete basis one must include zero frequency unphysical solutions. As we neglect the contribution of remote bands in our analysis, which the zero frequency solutions certainly are, no significant additional error is to be expected.

$$\Lambda_{c,\mathbf{k}\sim\mathbf{k}_{X_i}} = \Lambda_{c,\mathbf{k}_X} + |\Delta\mathbf{k}|^2 \left(\tilde{\eta}_{o,\mathbf{0}} - \tilde{\eta}_{o,2\mathbf{k}_X} \right) + \frac{4|(\Delta\mathbf{k} \cdot \mathbf{k}_{X_i})|^2 (\tilde{\eta}_{o,\mathbf{0}})^2}{\Delta\Lambda_X}, \quad (1.79)$$

where the index i has been dropped from \mathbf{k}_{X_i} in those quantities that have the same value for each element of the $\star\mathbf{k}$.

The bandgap at the X -point, $\Delta\Lambda_X$, may also be approximately determined in terms of the Fourier coefficients $\tilde{\eta}_{o,\mathbf{G}}$. The magnetic field eigenoperator \hat{L}_H can be written as,

$$\hat{L}_H = -\tilde{\eta}_{o,\mathbf{0}}\nabla^2 - \sum_{\mathbf{G}\neq\mathbf{0}} \tilde{\eta}_{o,\mathbf{G}} e^{i\mathbf{G}\cdot\mathbf{r}} (\nabla^2 + i\tilde{\eta}_{o,\mathbf{G}}\mathbf{G}\cdot\nabla). \quad (1.80)$$

Treating $\Delta\eta_o = \sum_{\mathbf{G}\neq\mathbf{0}} \tilde{\eta}_{o,\mathbf{G}} e^{i\mathbf{G}\cdot\mathbf{r}}$ as a perturbation to the average dielectric $\tilde{\eta}_{o,\mathbf{0}}$, and considering only the coupling between the forward and backward normalized plane wave states at the X -point, $(|\mathbf{k}_{X_i}\rangle, |-\mathbf{k}_{X_i}\rangle)$, results in the following two band magnetic field eigenoperator:

$$\hat{L}_H^{X_i} = \begin{pmatrix} \tilde{\eta}_{o,\mathbf{0}}|\mathbf{k}_X|^2 & -\tilde{\eta}_{o,2\mathbf{k}_X}|\mathbf{k}_X|^2 \\ -\tilde{\eta}_{o,2\mathbf{k}_X}|\mathbf{k}_X|^2 & \tilde{\eta}_{o,\mathbf{0}}|\mathbf{k}_X|^2 \end{pmatrix}. \quad (1.81)$$

The eigenvalues of $\hat{L}_H^{X_i}$ are $\tilde{\eta}_{o,\mathbf{0}}|\mathbf{k}_X|^2 \pm (\tilde{\eta}_{o,2\mathbf{k}_X})|\mathbf{k}_X|^2$, which gives for the bandgap, $\Delta\Lambda_X = 2(\tilde{\eta}_{o,2\mathbf{k}_X})|\mathbf{k}_X|^2$.

Choosing a coordinate basis $\hat{\mathbf{x}}_i$ with \hat{x}_i orthogonal to \mathbf{k}_{X_i} and \hat{y}_i parallel to \mathbf{k}_{X_i} , allows us to write for the local bandstructure of the conduction band in the vicinity of the X_i -point,

$$\Lambda_{c,\mathbf{k}\sim\mathbf{k}_{X_i}} = \Lambda_{c,\mathbf{k}_X} + \frac{\Delta\mathbf{k}_{x_i}^2}{m_{c,X,x_i}^*} + \frac{\Delta\mathbf{k}_{y_i}^2}{m_{c,X,y_i}^*}, \quad (1.82)$$

with effective ‘‘masses’’⁶ defined as,

⁶We use the term ‘‘mass’’ here in analogy to solid-state physics where the curvature of the bandstructure is related to the inverse of an effective electron mass. m^* as defined here is unitless.

$$\begin{aligned}\frac{1}{m_{c,X,x_i}^*} &= \tilde{\eta}_{o,\mathbf{0}} \left(1 - \frac{\tilde{\eta}_{o,2\mathbf{k}_X}}{\tilde{\eta}_{o,\mathbf{0}}} \right) \\ \frac{1}{m_{c,X,y_i}^*} &= \tilde{\eta}_{o,\mathbf{0}} \left(1 - \frac{\tilde{\eta}_{o,2\mathbf{k}_X}}{\tilde{\eta}_{o,\mathbf{0}}} + \frac{2\tilde{\eta}_{o,\mathbf{0}}}{\tilde{\eta}_{o,2\mathbf{k}_X}} \right).\end{aligned}\tag{1.83}$$

For a PC formed from dielectric materials with real refractive indices greater than that of vacuum, $0 \leq \eta_o(\mathbf{r}) \leq 1$. Consequently, $\tilde{\eta}_{o,\mathbf{0}} \geq 0$ and $\tilde{\eta}_{o,\mathbf{0}} \geq 2\tilde{\eta}_{o,\mathbf{G}}$ for all \mathbf{G} . The effective masses for the conduction band at the X -point are thus both positive.

Evaluating the scalar and vector coupling matrix elements using the X_i -point conduction band modes of equation (1.71) gives: $K_{l,l}(\mathbf{k}_{X_i}, \mathbf{k}_{X_i}, \mathbf{0}) = |\mathbf{k}_X|^2$ and $\mathbf{L}_{l,l}(\mathbf{k}_{X_i}, \mathbf{k}_{X_i}, \mathbf{0}) = \mathbf{0}$. Substituting these coupling matrix elements into equation (1.66), the effective Wannier potential is,

$$\Delta\eta'_{i,i}(\mathbf{r}) = |\mathbf{k}_X|^2 \Delta\eta(\mathbf{r}).\tag{1.84}$$

Lastly, upon substituting the local bandstructure of equation (1.82) and the effective Wannier potential of equation (1.84) into equation (1.67), we have for the Wannier equation of the conduction band envelope at the i th X -point:

$$\left((\Lambda_d - \Lambda_{c,\mathbf{k}_X}) - \left(\frac{-\nabla_{x_i}^2}{m_{c,X,x_i}^*} + \frac{-\nabla_{y_i}^2}{m_{c,X,y_i}^*} + |\mathbf{k}_X|^2 \Delta\eta(\mathbf{r}) \right) \right) \Gamma_{c,\mathbf{k}_{X_i}}(\mathbf{r}) = 0.\tag{1.85}$$

We now see from the Wannier-like equation for the conduction band edge at the X -point that as a result of the positive effective mass coefficients, localized resonant modes will form for perturbations to the hexagonal lattice in which $\Delta\eta(\mathbf{r})$ is locally reduced, that is for which the refractive index is locally *increased*.

Here we consider a defect which results in an approximate harmonic perturbation potential. By appropriately varying the hole radii of a photonic crystal consisting of a hexagonal array of air holes in a host dielectric material, the inverse of the filling fraction of the hexagonal crystal can be graded in a roughly parabolic fashion. The filling fraction of the lattice, f , as a function of air hole radius is,

$$f = 1 - \frac{2\pi}{\sqrt{3}} \left(\frac{r}{a}\right)^2, \quad (1.86)$$

where r is the hole radius and a is the nearest neighbor distance between holes of the hexagonal lattice. For a host dielectric material of refractive index n_o , the average dielectric constant of the patterned crystal is $\bar{\epsilon} = f(n_o)^2$. The slowly varying envelope of η_o ($\bar{\eta}_o$), neglecting rapid variations on the scale of the lattice spacing, is proportional to $1/f$, $\bar{\eta}_o = (n_o)^{-2}/f$. For an approximate harmonic potential then, the filling fraction of the lattice should vary as,

$$\frac{1}{f(\rho)} = \frac{1}{f_o} + k \left(\frac{\rho}{a}\right)^2, \quad (1.87)$$

with ρ representing the radial distance from the center of the defect, f_o the filling fraction given by the air hole radius at the center of the defect, and k the lattice grading coefficient. The filling fraction as used here is a local approximation, based upon the local hole radius, of the true filling fraction of a crystal lattice. The resulting slowly varying envelope of the effective Wannier potential is,

$$\overline{\Delta\eta'}_{i,i}(\rho) = k \left(\frac{\rho}{a}\right)^2 \left(\frac{|\mathbf{k}_X|}{n_o}\right)^2. \quad (1.88)$$

The ground state solution to equation (1.85) with the harmonic effective potential of equation (1.88) is the 2D Gaussian,

$$\Gamma_{c,\mathbf{k}_X}(\mathbf{r}) = \exp\left[-(x_i^2/\kappa^2 + y_i^2/\gamma^2)\right], \quad (1.89)$$

with decay constants,

$$\begin{aligned} \frac{1}{\kappa^2} &= \frac{1}{2} (\bar{k} m_{c,X,x_i}^*)^{\frac{1}{2}}, \\ \frac{1}{\gamma^2} &= \frac{1}{2} (\bar{k} m_{c,X,y_i}^*)^{\frac{1}{2}}, \end{aligned} \quad (1.90)$$

where $\bar{k} = k(|\mathbf{k}_X|/an_o)^2$.

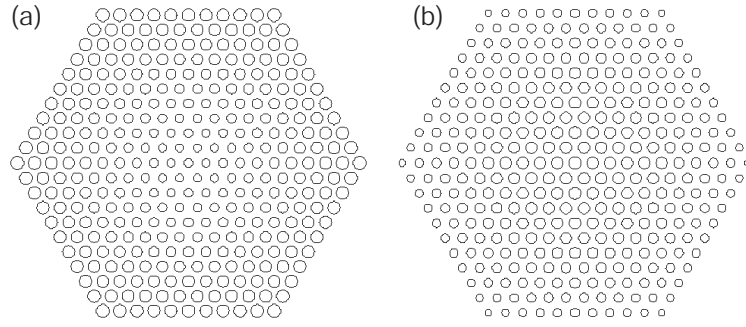


Figure 1.16: (a) Graded hexagonal lattice donor-type cavity, (b) graded hexagonal lattice acceptor-type cavity (parameters are given in table 1.4).

Table 1.4: Hexagonal PC parameters for the donor- and acceptor-type defect cavities.

cavity	n_o	$\left(\frac{r}{a}\right)_o$	f_o	k	\bar{k}/a^2	$\left(\frac{r}{a}\right)_e$	$\frac{\tilde{\eta}_{o,2k_X}}{\tilde{\eta}_{o,0}}$
donor	2.65	0.25	0.77	0.01	0.019	0.4	0.294
acc.	2.65	0.35	0.56	-0.006	0.015	0.20	0.23

From equation (1.86), in order to obtain the parabolic grade in filling fraction, the normalized hole radius of the defect cavity must vary with ρ as,

$$\left(\frac{r}{a}\right)^2 = \frac{\sqrt{3}}{2\pi} \left(1 - f_o \frac{1}{1 + f_o k (\rho/a)^2}\right). \quad (1.91)$$

With grading parameters given in table 1.4, the donor-type defect cavity we consider here is plotted in fig. 1.16(a). The calculated parameters of the approximate envelope function for the donor modes of this defect cavity are given in table 1.5.

The point group symmetry of the donor-type defect cavity of fig. 1.16(a) centered about point

Table 1.5: Donor mode (X -point) ground state Wannier envelope parameters.

m_{c,X,x_i}^*	m_{c,X,y_i}^*	$\frac{\kappa}{a}$	$\frac{\gamma}{a}$
7.7	0.72	2.3	4.1

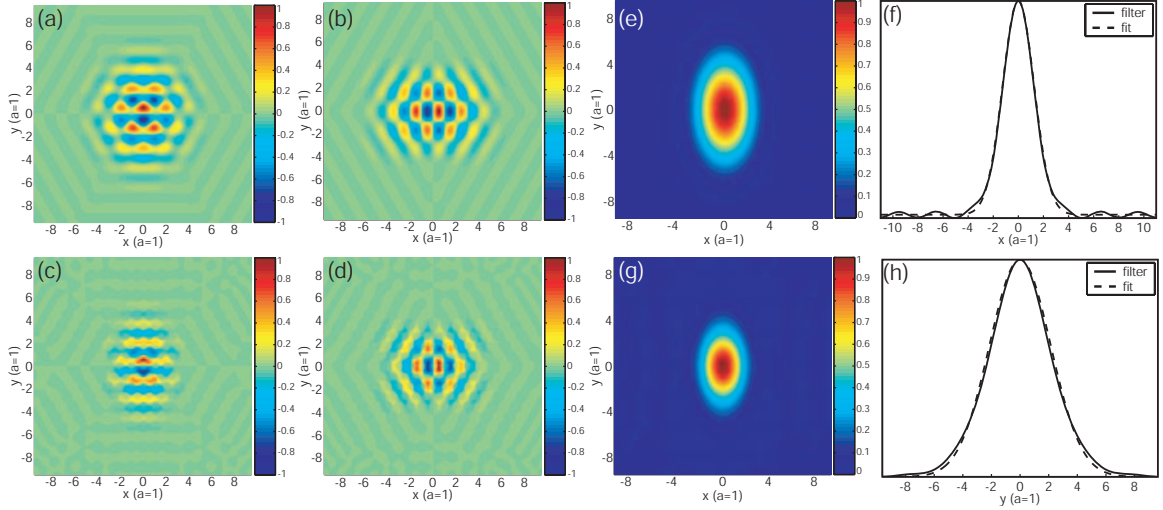


Figure 1.17: Magnetic field (\hat{z} -component) plot of the donor modes of the graded hexagonal donor-type cavity: (a) symmetry analysis $H_{E_{1,1}}^{a,d1}$ (x -dipole) mode, (b) symmetry analysis $H_{E_{1,2}}^{a,d1}$ (y -dipole) mode, (c) FDTD simulated x -dipole mode, and (d) FDTD simulated y -dipole mode. Comparison of: (e) Wannier and (g) FDTD envelope functions for $\mathbf{H}_{E_{1,1}}^{a,d1}$ (x -dipole) donor mode. (f) and (h) show line scans of the FDTD filtered envelope (solid line) along the \hat{x} - and \hat{y} -directions, respectively. The Gaussian fit to the FDTD envelope along these principal directions are also plotted (dashed line).

a of the hexagonal lattice is that of the underlying hexagonal lattice, C_{6v} . A set of basis functions for the localized conduction band donor modes was given in Equation 1.16, and has been rewritten here to include the conduction band envelope functions $\Gamma_{c,\mathbf{k}_{X_i}}$:

$$\begin{aligned}
 \mathbf{H}_{B_1''}^{a,d1} &= |c_{X_1}\rangle\Gamma_{c,\mathbf{k}_{X_1}} - |c_{X_2}\rangle\Gamma_{c,\mathbf{k}_{X_2}} + |c_{X_3}\rangle\Gamma_{c,\mathbf{k}_{X_3}}, \\
 \mathbf{H}_{E_{1,1}}^{a,d1} &= 2|c_{X_1}\rangle\Gamma_{c,\mathbf{k}_{X_1}} + |c_{X_2}\rangle\Gamma_{c,\mathbf{k}_{X_2}} - |c_{X_3}\rangle\Gamma_{c,\mathbf{k}_{X_3}}, \\
 \mathbf{H}_{E_{1,2}}^{a,d1} &= |c_{X_2}\rangle\Gamma_{c,\mathbf{k}_{X_2}} + |c_{X_3}\rangle\Gamma_{c,\mathbf{k}_{X_3}},
 \end{aligned} \tag{1.92}$$

In fig. 1.17(a)-(b) the magnetic field intensity is plotted for the dipole-like modes of the E_1 IRREP with envelope functions given by the $\Gamma_{c,\mathbf{k}_{X_i}}$ of equation (1.89). The calculated decay parameters for the Gaussian $\Gamma_{c,\mathbf{k}_{X_i}}$ are tabulated in table 1.5. Note that the coefficients of the expansion for each donor mode (c_i) are determined solely by the transformation properties of the basis CB_X^a ; the envelope functions transform effectively as the identity and do not modify the expansion coefficients.

For comparison, 2D FDTD simulations were performed on the donor-type cavity of fig. 1.16(a). Plots of the FDTD calculated magnetic field patterns (and their Fourier transforms) of the two modes most deep within the first order bandgap are given in fig. 1.17(c)-(d). The modes transform as the

Table 1.6: FDTD calculated mode envelope parameters.

mode	$\frac{\kappa}{a} (\frac{\kappa_x}{a})$	$\frac{\gamma}{a} (\frac{\kappa_y}{a})$
$\mathbf{H}_{E_1,1}^{a,d1}$	1.77	3.02
$\mathbf{H}_{A_2}^{a,a1}$	4.65	4.52
$\mathbf{H}_{B_2}^{a,a1}$	5.29	4.48

B_1'' and B_2'' IRREPs of the C_{2v} point group (the FDTD simulation was performed with mirror plane symmetries to reduce the size of the computation, thus projecting the modes onto the C_{2v} IRREPs), equivalent to the \hat{x} and \hat{y} basis of the C_{6v} IRREP E_1 (the basis chosen for modes $\mathbf{H}_{E_1,1}^{a,d1}$ and $\mathbf{H}_{E_1,2}^{a,d1}$). The FDTD generated field patterns show good correspondence with the field patterns of the approximate symmetry analysis (fig. 1.17(a)-(b)).

A more quantitative estimate of the envelope of the FDTD-generated localized modes can be obtained by considering the form of the approximate symmetry analysis modes of equation (1.92). Multiplying a donor mode which contains a dominant Fourier component at \mathbf{k}_{X_i} by $\cos(\mathbf{k}_{X_i} \cdot \mathbf{r}^a)$ will produce a term proportional to $\Gamma_{c,\mathbf{k}_{X_i}}$, thus shifting the envelope to the origin in Fourier space. Applying a low-pass spatial filter to the product of the mode and the cosine function will then leave only the envelope corresponding to $\Gamma_{c,\mathbf{k}_{X_i}}$. In fig. 1.17(f)-(h) we plot the result of such a procedure applied to the FDTD calculated $\mathbf{H}_{E_1,1}^{a,d1}$ (x -dipole) mode (fig. 1.17(e) shows a plot of the envelope calculated using the Wannier-like equation). The FDTD generated envelope is oriented parallel to \mathbf{k}_{X_1} , and as can be seen from fig. 1.17(f),(h) is Gaussian in nature. The fit decay parameters along \hat{x}_i and \hat{y}_i directions are given in table 1.6, and although smaller than estimated (table 1.5), they are in nearly the precise ratio predicted by the Wannier equation

1.2.3.2 Acceptor modes at the J -point

As mentioned above, the valence band edge of the fundamental bandgap for TE-like modes occurs at the J -point of the reciprocal lattice for the hexagonal PC. From section 1.1.2.2, the approximate form for the band edge states at the J -point is:

$$VB_J^a = \begin{pmatrix} v_{J_1} \\ v_{J_2} \end{pmatrix} = \hat{z} \begin{pmatrix} e^{i\mathbf{k}_{J_1} \cdot \mathbf{r}^a} + e^{i\mathbf{k}_{J_3} \cdot \mathbf{r}^a} + e^{i\mathbf{k}_{J_5} \cdot \mathbf{r}^a} \\ e^{i\mathbf{k}_{J_2} \cdot \mathbf{r}^a} + e^{i\mathbf{k}_{J_4} \cdot \mathbf{r}^a} + e^{i\mathbf{k}_{J_6} \cdot \mathbf{r}^a} \end{pmatrix}, \quad (1.93)$$

for valence band modes, and

$$CB_J^a = \begin{pmatrix} c1_{J_1} \\ c2_{J_1} \\ c1_{J_2} \\ c2_{J_2} \end{pmatrix} = \hat{z} \begin{pmatrix} e^{-ik_{J_1} \cdot \mathbf{r}^a} + e^{-ik_{J_3} \cdot \mathbf{r}^a} - 2e^{-ik_{J_5} \cdot \mathbf{r}^a} \\ e^{-ik_{J_1} \cdot \mathbf{r}^a} - e^{-ik_{J_3} \cdot \mathbf{r}^a} \\ e^{-ik_{J_2} \cdot \mathbf{r}^a} + e^{-ik_{J_4} \cdot \mathbf{r}^a} - 2e^{-ik_{J_6} \cdot \mathbf{r}^a} \\ e^{-ik_{J_2} \cdot \mathbf{r}^a} - e^{-ik_{J_4} \cdot \mathbf{r}^a} \end{pmatrix}. \quad (1.94)$$

for conduction band modes. The normalized periodic functions of the above Bloch modes are,

$$\begin{aligned} h_{v, \mathbf{k}_{J_1}} &= \frac{1}{\sqrt{3}} (1 + e^{-i2\mathbf{k}_{X_1} \cdot \mathbf{r}^a} + e^{-i2\mathbf{k}_{X_2} \cdot \mathbf{r}^a}), \\ h_{v, \mathbf{k}_{J_2}} &= \frac{1}{\sqrt{3}} (1 + e^{-i2\mathbf{k}_{X_2} \cdot \mathbf{r}^a} + e^{-i2\mathbf{k}_{X_3} \cdot \mathbf{r}^a}), \end{aligned} \quad (1.95)$$

$$\begin{aligned} h_{c1, \mathbf{k}_{J_1}} &= \frac{1}{\sqrt{6}} (1 + e^{-i2\mathbf{k}_{X_1} \cdot \mathbf{r}^a} - 2e^{-i2\mathbf{k}_{X_2} \cdot \mathbf{r}^a}), \\ h_{c1, \mathbf{k}_{J_2}} &= \frac{1}{\sqrt{6}} (1 + e^{-i2\mathbf{k}_{X_2} \cdot \mathbf{r}^a} - 2e^{-i2\mathbf{k}_{X_3} \cdot \mathbf{r}^a}), \end{aligned} \quad (1.96)$$

$$\begin{aligned} h_{c2, \mathbf{k}_{J_1}} &= \frac{1}{\sqrt{2}} (1 - e^{-i2\mathbf{k}_{X_1} \cdot \mathbf{r}^a}), \\ h_{c2, \mathbf{k}_{J_2}} &= \frac{1}{\sqrt{2}} (1 - e^{-i2\mathbf{k}_{X_2} \cdot \mathbf{r}^a}). \end{aligned} \quad (1.97)$$

The local bandstructure for the valence band at the J_1 -point, upon evaluating equation (1.76) using the approximate J_1 -point valence and conduction band modes above, is

$$\begin{aligned}
\Lambda_{v, \mathbf{k} \sim \mathbf{k}_{J_1}} &= \Lambda_{v, \mathbf{k}_J} + |\Delta \mathbf{k}|^2 \left(\tilde{\eta}_{o, \mathbf{0}} + 2\tilde{\eta}_{o, 2\mathbf{k}_X} \right) \\
&\quad - \left(|\Delta \mathbf{k} \cdot \mathbf{k}_{J_2}|^2 \frac{\left(2(\tilde{\eta}_{o, \mathbf{0}})^2 + \frac{1}{2}(\tilde{\eta}_{o, 2\mathbf{k}_X})^2 + 2(\tilde{\eta}_{o, \mathbf{0}})(\tilde{\eta}_{o, 2\mathbf{k}_X}) \right)}{\Delta \Lambda_J} \right. \\
&\quad \left. + \frac{4}{3} |\Delta \mathbf{k} \cdot \mathbf{k}_{X_1}|^2 \frac{\left(2(\tilde{\eta}_{o, \mathbf{0}})^2 + \frac{1}{2}(\tilde{\eta}_{o, 2\mathbf{k}_X})^2 + 2(\tilde{\eta}_{o, \mathbf{0}})(\tilde{\eta}_{o, 2\mathbf{k}_X}) \right)}{\Delta \Lambda_J} \right) \\
&= \Lambda_{v, \mathbf{k}_J} + |\Delta \mathbf{k}|^2 \left(\tilde{\eta}_{o, \mathbf{0}} + 2\tilde{\eta}_{o, 2\mathbf{k}_X} - \frac{|\mathbf{k}_J|^2 \left(2(\tilde{\eta}_{o, \mathbf{0}})^2 + \frac{1}{2}(\tilde{\eta}_{o, 2\mathbf{k}_X})^2 + 2(\tilde{\eta}_{o, \mathbf{0}})(\tilde{\eta}_{o, 2\mathbf{k}_X}) \right)}{\Delta \Lambda_J} \right),
\end{aligned} \tag{1.98}$$

where $\Delta \mathbf{k} = \mathbf{k} - \mathbf{k}_{J_1}$. To second order in the elements of $\Delta \mathbf{k}$, the local bandstructure around the J_1 -point of the valence band is centro-symmetric. As a result, the local bandstructure in the neighborhood of each of the J points of the $\star \mathbf{k}$ is also given by equation (1.98). In order to determine the sign of the curvature of the valence band, the bandgap at the J -point, $\Delta \Lambda_J$, is evaluated using a similar procedure as for the bandgap at the X -point. The three band eigenoperator, in the normalized plane wave basis of $(|\mathbf{k}_{J_1}\rangle, |\mathbf{k}_{J_3}\rangle, |\mathbf{k}_{J_5}\rangle)$, is:

$$\hat{L}_H^{J_1} = |\mathbf{k}_J|^2 \begin{pmatrix} \tilde{\eta}_{o, \mathbf{0}} & -\frac{1}{2}\tilde{\eta}_{o, 2\mathbf{k}_X} & -\frac{1}{2}\tilde{\eta}_{o, 2\mathbf{k}_X} \\ -\frac{1}{2}\tilde{\eta}_{o, 2\mathbf{k}_X} & \tilde{\eta}_{o, \mathbf{0}} & -\frac{1}{2}\tilde{\eta}_{o, 2\mathbf{k}_X} \\ -\frac{1}{2}\tilde{\eta}_{o, 2\mathbf{k}_X} & -\frac{1}{2}\tilde{\eta}_{o, 2\mathbf{k}_X} & \tilde{\eta}_{o, \mathbf{0}} \end{pmatrix}. \tag{1.99}$$

The eigenvalues of $\hat{L}_H^{J_1}$ consist of the single eigenvalue $\Lambda_{v, \mathbf{k}_J} = |\mathbf{k}_J|^2(\tilde{\eta}_{o, \mathbf{0}} - \tilde{\eta}_{o, 2\mathbf{k}_X})$, and the double eigenvalue $\Lambda_{c, \mathbf{k}_J} = |\mathbf{k}_J|^2(\tilde{\eta}_{o, \mathbf{0}} + \tilde{\eta}_{o, 2\mathbf{k}_X}/2)$. The bandgap at the J -point is then, $\Delta \Lambda_J = (3/2)\tilde{\eta}_{o, 2\mathbf{k}_X} |\mathbf{k}_J|^2$. Substituting this value of $\Delta \Lambda_J$ into the equation (1.98) we have for the local bandstructure at each of the J -points,

$$\Lambda_{v, \mathbf{k} \sim \mathbf{k}_J} = \Lambda_{v, \mathbf{k}_J} + \frac{|\Delta \mathbf{k}|^2}{m_{v, J}^*}. \tag{1.100}$$

where the effective mass of the valence band is,

$$\frac{1}{m_{v,J}^*} = -\frac{1}{3}\tilde{\eta}_{o,\mathbf{0}} \left(1 + 3\frac{\tilde{\eta}_{o,2\mathbf{k}_X}}{\tilde{\eta}_{o,\mathbf{0}}} + \frac{4((\tilde{\eta}_{o,\mathbf{0}})^2 - 2(\tilde{\eta}_{o,2\mathbf{k}_X})^2)}{(\tilde{\eta}_{o,\mathbf{0}})(\tilde{\eta}_{o,2\mathbf{k}_X})} \right). \quad (1.101)$$

As expected for the valence band, the effective mass is negative at the J -point.

The scalar and vector coupling matrix elements, evaluated using the J_1 -point valence band mode of equation (1.95), are: $K_{v,v}(\mathbf{k}_{J_1}, \mathbf{k}_{J_1}, \mathbf{0}) = |\mathbf{k}_J|^2$ and $\mathbf{L}_{v,v}(\mathbf{k}_{J_1}, \mathbf{k}_{J_1}, \mathbf{0}) = \mathbf{0}$. The resulting effective Wannier potential at the J -point is given by,

$$\Delta\eta'_{i,i}(\mathbf{r}) = |\mathbf{k}_J|^2 \Delta\eta(\mathbf{r}). \quad (1.102)$$

With the local bandstructure of equation (1.100) and the effective potential of equation (1.102), the Wannier equation of the valence band envelope at the J -point is:

$$\left((\Lambda_d - \Lambda_{v,\mathbf{k}_J}) - \left(\frac{-\nabla^2}{m_{v,J}^*} + |\mathbf{k}_J|^2 \Delta\eta(\mathbf{r}) \right) \right) \Gamma_{v,\mathbf{k}_J}(\mathbf{r}) = 0. \quad (1.103)$$

Due to the negative effective mass coefficient, localized resonant modes will form for local perturbations to the hexagonal lattice in which the refractive index is locally *decreased*. The acceptor-type defect is taken to consist of a grade in the radius of the air holes of the hexagonal crystal as defined in equation (1.91), with grading coefficient $k = -0.006$. The values of the parameters of the acceptor-type cavity are given in table 1.4 and a plot of the acceptor-type cavity is shown in fig. 1.16(b).

As was the case for the donor-type cavity, this grade in the hole radius results in an approximate parabolic potential well. Therefore, we take as our approximate ground state envelope function the Gaussian,

$$\Gamma_{v,\mathbf{k}_J}(\mathbf{r}) = \exp\left[-(\rho/\kappa)^2\right], \quad (1.104)$$

with $\rho = |\mathbf{r}_\perp|$ the in-plane radius, and κ a single parameter decay constant given by,

Table 1.7: Acceptor mode (J -point) ground state Wannier envelope parameters

$m_{v,J}^*$	$\frac{\kappa}{a} = \frac{\kappa_x}{a} = \frac{\kappa_y}{a}$
-0.68	4.44

$$\frac{1}{\kappa^2} = \frac{1}{2} (\bar{k} |m_{v,J}^*|)^{\frac{1}{2}}, \quad (1.105)$$

where $\bar{k} = |k|(|\mathbf{k}_J|/an_o)^2$. The value of κ/a as calculated for the acceptor-type defect of fig. 1.16(b) is given in table 1.7.

From equation (1.20), we have a form for acceptor modes formed at the J -point of the hexagonal lattice. Rewriting these equations to include the Wannier envelope functions, we arrive at:

$$\begin{aligned} \mathbf{H}_{A_2''}^{a,a1} &= |v_{J_1}\rangle \Gamma_{v,\mathbf{k}_J} + |v_{J_2}\rangle \Gamma_{v,\mathbf{k}_J} \\ &\propto \hat{z} (\cos(\mathbf{k}_{J_1} \cdot \mathbf{r}) + \cos(\mathbf{k}_{J_2} \cdot \mathbf{r}) + \cos(\mathbf{k}_{J_3} \cdot \mathbf{r})) \Gamma_{v,\mathbf{k}_J}, \\ \mathbf{H}_{B_2''}^{a,a1} &= |v_{J_1}\rangle \Gamma_{v,\mathbf{k}_J} - |v_{J_2}\rangle \Gamma_{v,\mathbf{k}_J} \\ &\propto \hat{z} (\sin(\mathbf{k}_{J_1} \cdot \mathbf{r}) + \sin(\mathbf{k}_{J_2} \cdot \mathbf{r}) + \sin(\mathbf{k}_{J_3} \cdot \mathbf{r})) \Gamma_{v,\mathbf{k}_J}, \end{aligned} \quad (1.106)$$

where the Γ_{v,\mathbf{k}_J} are equivalent for each element of the $\star\mathbf{k}$ due to the isotropic effective mass of the J -point valence band. A plot of the magnetic field (\hat{z} -component) for the symmetry basis modes $\mathbf{H}_{A_2''}^{a,a1}$ and $\mathbf{H}_{B_2''}^{a,a1}$ are given in fig. 1.18(a)-(b).

2D FDTD simulations of the acceptor-type cavity of fig. 1.16(b) and table 1.4 were also performed. The two deepest modes within the first order bandgap are found to be of A_2'' and B_2'' symmetry, the same symmetry as the modes predicted by the approximate analysis. Plots of the FDTD calculated magnetic field patterns of these modes are given in fig. 1.18(c)-(d), again showing a strong resemblance to the approximately generated field patterns. Figure 1.18(e)-(h) shows a series of plots of the envelope ($\Gamma_{v,\mathbf{k}_{J_1}}$) of the acceptor mode $\mathbf{H}_{A_2''}^{a,a1}$. The size and shape (isotropic) of the FDTD calculated mode envelope corresponds very nicely with the approximate Wannier envelope as can be seen by the Gaussian fits in fig. 1.18(f)-(h) and the values of the fit decay constants given in table 1.6. A similar envelope was extracted for mode $\mathbf{H}_{B_2''}^{a,a1}$, with its fit decay constants given in

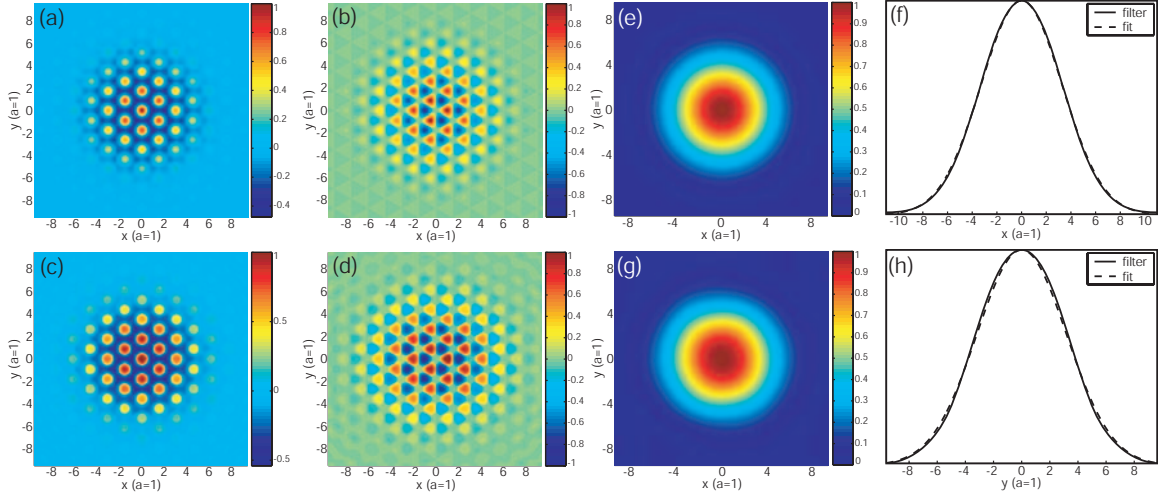


Figure 1.18: Magnetic field (\hat{z} -component) plots of the acceptor modes of the graded hexagonal lattice acceptor-type cavity: (a) symmetry analysis A_2'' mode, (b) symmetry analysis B_2'' mode, (c) FDTD A_2'' mode, and (d) FDTD B_2'' mode. Comparison of: (e) Wannier (see table 1.7) and (g) FDTD envelope functions for the $\mathbf{H}_{A_2}^{a,a1}$ acceptor mode. (f) and (h) show line scans of the FDTD filtered envelope (solid line) along the \hat{x} - and \hat{y} -directions, respectively. The Gaussian fit to the FDTD envelope along these principal directions are also plotted (dashed line).

table 1.6 as well.